



Available online at [www.sciencedirect.com](http://www.sciencedirect.com)

**ScienceDirect**

Comput. Methods Appl. Mech. Engrg. 401 (2022) 115614

**Computer methods  
in applied  
mechanics and  
engineering**

[www.elsevier.com/locate/cma](http://www.elsevier.com/locate/cma)

# A five-phase approach, SPH framework and applications for predictions of seepage-induced internal erosion and failure in unsaturated/saturated porous media

Guodong Ma<sup>a</sup>, Ha H. Bui<sup>a,\*</sup>, Yanjian Lian<sup>a</sup>, Khoa M. Tran<sup>a</sup>, Giang D. Nguyen<sup>b</sup>

<sup>a</sup> Department of Civil Engineering, Monash University, Melbourne, Australia

<sup>b</sup> School of Civil, Environmental & Mining Engineering, University of Adelaide, Adelaide, Australia

Received 1 March 2022; received in revised form 23 August 2022; accepted 24 August 2022

Available online 30 September 2022

## Abstract

Seepage-induced internal erosion and failure in unsaturated/saturated porous media is challenging for computational simulations as they involve the behaviour, interactions (solid, air, water) and transformation (fluidisation and deposition of fines grains) of different phases. Tackling this challenging problem requires correct mathematical descriptions of phase interactions and transformation together with a robust computational framework, both of which are addressed in this paper. The new mathematical model and coupled governing equations based on the continuum mixture theory enable the use of a single set of SPH particles for the descriptions of behaviour, interactions and phase transformation of all five phases of the porous media (soil skeleton, erodible fines particles, fluidised particles, water, and air), including the effect of both saturation and erosion on the shear strength of porous media. A fully explicit and stabilised SPH framework that allows accurate SPH approximations of spatial gradients is proposed for the numerical solutions of coupled governing equations. The proposed computational framework performs well in benchmark tests against available analytical and numerical solutions and achieved reasonable agreements with experiments. Numerical results obtained from the predictions of seepage-induced erosion and failure demonstrate that the proposed computational framework is efficient for addressing challenging problems involving coupled flow-deformation, seepage-induced internal erosions, and large deformation failures of unsaturated/saturated porous media.

© 2022 Elsevier B.V. All rights reserved.

**Keywords:** Unsaturated porous media; Seepage flow; Internal erosion; Smooth particle hydrodynamics; Large deformation and failure

## 1. Introduction

Soil mixture is usually composed of soil skeletons (coarse particles), fines particles, air, and water. When water seepages through pores, fines particles can be eroded into the water and become fluidised particles, which can be subsequently transported and deposited inside pores. This process is commonly known as the seepage-induced internal erosion process. It can alter hydraulic and mechanical properties of soils (e.g., gradation, fines content, porosity, permeability, shear strength), leading to a series of significant damages, such as piping,

\* Corresponding author.

E-mail address: [ha.bui@monash.edu](mailto:ha.bui@monash.edu) (H.H. Bui).

settlement, sinkholes, or landslides [1–3]. For example, nearly 46% of global embankment collapses were caused by seepage-induced internal erosion [3].

To understand failure mechanisms associated with seepage-induced erosion, many experimental studies have been conducted. For example, Skempton and Brogan [4] conducted separation-piping experiments and concluded that the critical hydraulic gradient was a third or a fifth of Terzaghi's critical upward hydraulic gradient [5]. Chang and Zhang [6] reported a similar conclusion when studying the critical hydraulic gradients of erosion under complex stress states using a triaxial permeameter. However, hydraulic gradients or seepage velocities are indirect factors contributing to the erosion, while fines content and porosity are considered as direct factors, both of which are hard to quantify and measure from standard experiments. To address this issue, 3D X-ray CT imaging experiments were adopted [7,8]. However, these tests are often time-consuming, high cost, and lack representativity. Laboratory-scale tests of embankment failure were also conducted [9–12] to study the complex behaviour of seepage-induced internal erosion and failure of earth structures. These tests have advantages in observing boundary value problems of transient seepage from unsaturated to fully saturated states, as well as the large deformation and failure of embankments caused by seepage erosion. However, the receptivity of these large-scale tests is often expensive and challenging, and thus from this point of view, numerical tools can be an excellent alternative to overcome these difficulties and complement experiments.

Several continuum mathematical models have been proposed in the past to study seepage-induced internal erosion. However, most of these mathematical models were presented at the conceptual level, and very few attempts were made to solve them for predictions of the complete failure of porous media caused by seepage erosion. For example, Vardoulakis et al. [13] established a continuum model consisting of three phases (i.e., solid, fluid, and fluidised solid particles) to study the sand production problem. This continuum model could depict the phase transformation between fluidised particles and solid particles as well as the concentration of fluidised particles, but fail to describe the variations of fines content. Furthermore, the deformation of solid phase was completely ignored in this model. Steeb et al. [14,15] established a four-phase continuum model for saturated porous media, in which the solid phase was separated into the erodible fines particles and non-erodible soil skeleton, while the fluid phase was separated into water and fluidised particles, so that phase interactions and transformation, as well as the concentration and fines content, were depicted. Although this framework represents a promising approach to dealing with internal erosion, no numerical attempts to solve these proposed coupled governing equations were reported in Steeb et al. [14,15]. Recently, several numerical attempts have been made to solve this four-phase erosion mathematical model using the finite element method (FEM) for engineering-scale applications. For example, Yang et al. [16,17] attempted to predict the 2D and 3D sinkhole problems induced by internal erosion using FEM, but no quantitative validations against analytical solutions or experiments were made. Lei et al. [18] and Zhang [19] extended Steeb's erosion model to account for unsaturated seepage flows and attempted to simulate the rainfall-induced erosion problem by FEM. However, their proposed model was incomplete as they did not consider the influence of internal erosion on the shear strength of soils and their coupling effects, among several other inconsistent governing equations. Furthermore, no validations with experiments were made, and large deformation of solid was also not considered in these works. Yang et al. [20] also conducted erosion and filtration of fine particles in granular media using finite difference method (FDM), and studied the influence of randomly distributed porosity and fines content on erosion process. These works highlight the soil heterogeneity [21], which will be considered in our future study.

Recently, Lei et al. [22] presented a material point method (MPM) framework to investigate rainfall-induced erosion and slope instability problems using a three-phase multi-species model, which was an extension of their previous erosion model (Lei et al. [18]). Their MPM framework was verified against a fundamental experiment of seepage-induced internal erosion (i.e., drainage tests) for 1D conditions. This MPM framework was subsequently used to study rainfall-induced slope failure problems without comparing them with any experiments. Similar to their previous studies, this three-phase multi-species model did not consider the effects of internal erosion on the mechanical strength of the materials, showing a lack of a complete model for internal erosion-induced failure. Furthermore, the consideration of a three-phase system limits their model from a complete description of phase interactions and phase transformations caused by internal erosion. Alternative to MPM, the Smoothed Particle Hydrodynamics (SPH) method has been well developed and successfully applied to solve many challenging geotechnical problems, including granular flows [23,24], slope collapses [23,25–30], landslides [31,32], debris flows [33,34], soil/fluid–structure interactions [35–40], fractures [41,42], and transient seepage flows [11,43–45].

Compared to MPM, SPH has more advantages in the sense that the method is a truly mesh-free method and does not require any background mesh to solve the governing equations. It shares the same library of continuum constitutive models with FEM and MPM, meaning that any existing continuum constitutive models can be straightforwardly adopted in SPH. Because of these features, SPH is in an excellent position to handle large-scale engineering applications involving large deformation and failure of geomaterials. It is also worth noting that the continuum numerical methods (e.g., FEM, PFEM, MPM, SPH) have some advantages in treating large-scale coupled solid deformation–fluid flow problems [46,47] over discrete element methods [48,49]. Therefore, the SPH method is preferred in this study to solve these mathematical models.

Despite several existing mathematical models for internal erosion, there is still a need to develop a complete and rigorous mathematical model for a complete description of complex phase interactions, phase transformations and strength reduction caused by internal erosion. In general, internal erosion mainly occurs in fully saturated soils, and thus it would be sufficient to consider the problem as a fully saturated porous mixture. However, such simplified computational models provide limited capabilities for solving general boundary value problems. For instance, most field applications related to internal erosion involve transient seepage flows, and the accurate prediction of the transient seepage flow in the porous medium plays a vital role in evaluating the stability of earth structures caused by internal erosion. For this reason, a more comprehensive mathematical model is required for broader engineering applications. In our view, a five-phase mathematical model is needed to provide enough flexibility for a more rigorous description of internal erosion in unsaturated/saturated porous media. Furthermore, no existing generic SPH framework is capable of simulating the fully coupled seepage erosion process and the induced large deformation failure behaviour of geomaterials. One of the key reasons that prevent these applications is that most existing computational frameworks, including FEM, MPM and SPH, often suffer from instability caused by significant pore-water pressure fluctuation when it comes to solving fully coupled problems [50–53]. In this paper, a five-phase mathematical model and a stabilised SPH framework are developed to address the above challenges and are subsequently used to solve seepage-induced erosions and failures of unsaturated/saturated porous media. To our best knowledge, they will be the first of their kind (i.e., mathematical model & SPH computational framework) capable of tackling several important aspects of seepage-erosion problems related to transient seepage flows, coupled flow-deformation, seepage-induced internal erosion, and soil degradation due to saturation and internal erosion process.

## 2. A continuum mathematical model for unsaturated erodible porous medium

### 2.1. Phase definitions and homogenisations

Let us consider a representative volume element (RVE) of a partially saturated porous medium undergoing internal erosion, as shown in Fig. 1(a). Assuming that the coarse fraction of the solid mixture ( $s$ ) in the system forms the soil skeleton ( $ss$ ) and is non-erodible, whilst the fines fraction of the solid mixture consists of erodible fines particles ( $se$ ), which can be eroded and turned into fluidised particles ( $sf$ ) and freely move together with the water ( $w$ ). Under this consideration, it is possible to consider the RVE as a five-phase material system, consisting of the soil skeleton ( $ss$ ), erodible-fines ( $se$ ), water ( $w$ ), air ( $a$ ) and fluidised-particle ( $sf$ ) phases, such that  $V_t = V_{ss} + V_{se} + V_w + V_a + V_{sf}$ , as shown in Fig. 1(b). The solid mixture ( $s$ ) is made of soil skeleton ( $ss$ ) and erodible-fines ( $se$ ) phases ( $V_s = V_{ss} + V_{se}$ ), whilst the fluid mixture ( $f$ ) is made of the water ( $w$ ) and fluidised-particle ( $sf$ ) phases ( $V_f = V_w + V_{sf}$ ). Under the action of external loads, each constituent moves with their corresponding mixture and shares the same velocity as the mixture. The mass exchange then occurs between the solid ( $s$ ) and fluid ( $f$ ) mixtures through an internal erosion process which turns erodible-fines ( $se$ ) to fluidised-particle ( $sf$ ) phases. In other words, the mass exchange only occurs between erodible-fines ( $se$ ) to fluidised-particle ( $sf$ ) phases. Furthermore, it is possible that fluidised-particle phase accumulated in the solid mixture and contributed to the erodible-fines phase during the internal erosion process (i.e., deposition). Other assumptions to simplify the mathematical description of our proposed system are:

- The system is isothermal, and Darcy's law is assumed valid for the transport of all fluid phases.
- Internal erosion mainly occurs inside the fully saturated porous media and its transition zone when the critical hydraulic gradient is met.

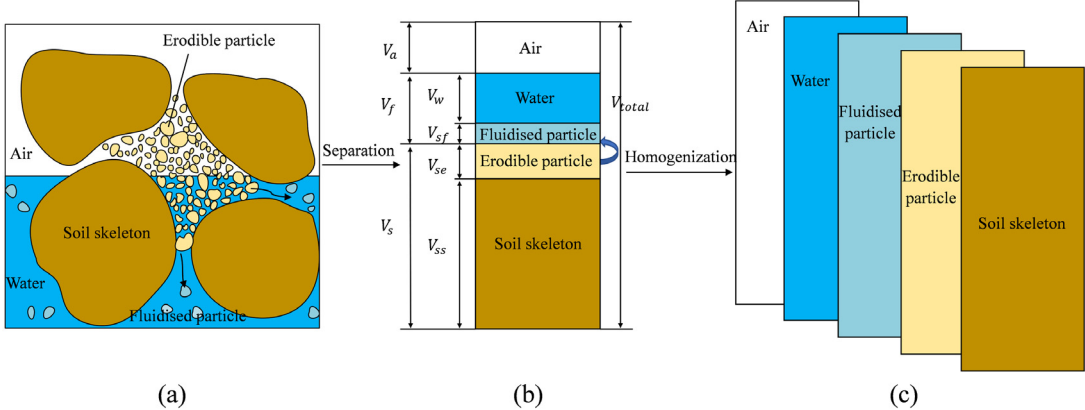


**Fig. 1.** Concept of a five-phase mathematical model.

- c. All fluid phases (i.e., water, air and fluidised-particle) are assumed to be continuous in the pore space and are in contact with solid phases. The air phase is connected to the atmosphere, and no mass transfer due to vaporisation/condensation is considered.
- d. Solid grains and fluidised particles are assumed to be incompressible, while water is assumed to be weakly compressible. In addition, all fluid phases inside the porous medium are assumed to be Newtonian fluid.
- e. Both water and fluidised-particle phases share the same intrinsic pressure of the fluid mixture (i.e.,  $\sigma_w = \sigma_{sf} = \sigma_f = -p_f \mathbf{I}$ ), whilst their partial stresses depend on their volume fractions.
- f. Both solid phases ( $ss, se$ ) and fluid phases ( $sf, w$ ) share the same velocity as the solid mixture ( $\mathbf{v}_{ss} = \mathbf{v}_{se} = \mathbf{v}_s$ ) and fluid mixture ( $\mathbf{v}_{sf} = \mathbf{v}_w = \mathbf{v}_f$ ).

Under the above assumptions, a homogenisation process can be now applied to the above five-phase system by assuming that each phase ( $\alpha = ss, se, w, a, sf$ ) can be treated as a continuum phase and will occupy the entire volume  $V$  of the RVE, as shown in Fig. 1(c). In this context, the proposed system is viewed as five independent overlapping continua (i.e., at every point, all phases are present at the same time), each of which has its own kinematics, mass and momentum and interacts with each other through general laws of physics (e.g., seepage forces and pore-pressure). The continuum mixture theory can be then adopted to establish the governing equations for this five-phase system.

In the context of the mixture theory, each phase has a volume fraction defined as  $n_\alpha = V_\alpha / V_t$ , which is subjected to the following constraint:

$$n_{ss} + n_{se} + n_w + n_{sf} + n_a = 1 \quad (1)$$

The fines content  $f_c = V_{se}/V_s$  and the solid concentration  $C = V_{sf}/V_f$  can also be defined to keep track of the mass loss and migration of fluidised particles caused by internal erosion, respectively. As a result, the volume fraction of each phase can be expressed as a function of these quantities:

$$\begin{aligned} n_{ss} &= (1 - f_c)(1 - \phi) & n_{se} &= f_c(1 - \phi) & n_w &= (1 - C)S_r\phi \\ n_{sf} &= CS_r\phi & n_a &= (1 - S_r)\phi \\ n_s &= (1 - \phi) & n_f &= S_r\phi \end{aligned} \quad (2)$$

where  $\phi$  is the porosity and  $S_r$  is the degree of saturation.

The definition of volume fractions gives rise to the partial density of  $\bar{\rho}_\alpha = \rho_\alpha n_\alpha$ , where  $\rho_\alpha$  is the intrinsic density of each phase  $\alpha$ , and all solid components (i.e.,  $sf, ss, se$ ) share the same intrinsic solid density ( $\rho_s$ ). The partial densities of the solid mixtures  $\bar{\rho}_s$  ( $ss, se$ ) and fluid mixtures  $\bar{\rho}_f$  ( $sf, w$ ) can be then defined as follows:

$$\bar{\rho}_s = \bar{\rho}_{ss} + \bar{\rho}_{se} = n_s \rho_s \quad (3)$$

$$\bar{\rho}_f = \bar{\rho}_w + \bar{\rho}_{sf} = n_f \rho_f = n_f [(1 - C)\rho_w + C\rho_s] \quad (4)$$

Eq. (4) indicates that the intrinsic density of the fluid mixture is a function of solid concentration and thus changes with internal erosion. This feature enables the proposed mathematical model to effectively account for the influences of internal erosion on the evolution of other physical quantities of the porous mixture, thanks to the proposed five-phase concept. Finally, the density of the entire mixture is the sum of all partial densities:

$$\rho_t = \bar{\rho}_s + \bar{\rho}_f + \bar{\rho}_a = \bar{\rho}_{ss} + \bar{\rho}_{se} + \bar{\rho}_w + \bar{\rho}_{sf} + \bar{\rho}_a \quad (5)$$

## 2.2. Definition of effective stress

One of the crucial questions concerning the partially saturated porous system is the definition of effective stress, which controls changes in volume and the strength of the porous system. Depending on the nature of a porous medium, which may consist of more than one fluid, the definition of effective stress may vary significantly. In general, the following versatile definition of effective stress for a porous medium is well accepted [54–57],

$$\sigma' = \sigma + B\bar{p}^f \mathbf{I} \quad (6)$$

where  $\sigma'$  is the effective stress carried by the solid mixture;  $\sigma$  is the total stress applied to the RVE;  $\bar{p}^f$  is the average pore fluid pressure of the entire RVE; and  $B$  is the Biot's compressibility coefficient, which is unity in this paper.

The key difference among various effective stress equations reported in the literature is the definition of average pore fluid pressure  $\bar{p}^f$  for a porous system consisting of more than one fluid. For a partially saturated porous system consisting of three-phase materials (i.e., solid, water and air phases), Bishop proposed the following well-known effective stress equation [57,58]:

$$\sigma' = (\sigma + p_a \mathbf{I}) - \chi(p_a - p_w) \mathbf{I} \quad (7)$$

where  $p_w$  and  $p_a$  are the pore-water and pore-air pressures, respectively; and  $\chi$  is the effective stress parameter, which has a value of 0 to 1 for dry and saturated soils, respectively.

Various attempts have been made to interpret and quantify  $\chi$  from both theories and experiments. Bishop originally adopted  $\chi$  to account for the difference in the contact surface between the pore fluids and the solid phase. However, Khalili et al. [59] argued that  $\chi$  should be a function of suction and proposed a well-known empirical relation, which fits well with the experimental data for a wide range of soils. On the other hand, for many applications in soil mechanics, it is sufficient to approximate  $\chi$  by the degrees of saturation  $S_r$  [60–63]. In fact, the replacement of  $\chi$  by the degrees of saturation can be theoretically achieved by establishing the required work input for unsaturated soils [61]. In this paper, the latter approach is adopted, though any form of effective stress equation following the general form of Eq. (6) can also be incorporated into our proposed mathematical framework. The derivation of this effective stress equation subjected to certain assumptions is briefly explained below, and a more rigorous approach to establish a work input for the proposed system will be explored in our future work. First, using the above definitions of volumetric fractions, the total stress tensor of the mixture can be written as follows [64,65]:

$$\sigma = \sum \bar{\sigma}_\alpha = \sum n_\alpha \sigma_\alpha \quad (8)$$

where  $\bar{\sigma}_\alpha$  and  $\sigma_\alpha$  are the partial and intrinsic stress tensors of phase  $\alpha$ , respectively. It is noted that, in the above total stress equation, the contribution due to diffusion and surface tension (i.e., contractile skin) has been neglected.

Next, by adopting the assumptions of fluid pressures are equal (i.e.,  $\sigma_w = \sigma_{sf} = \sigma_f = -p_f \mathbf{I}$ ). The total stress tensor of the entire mixture can be rewritten as:

$$\sigma = \bar{\sigma}_s - \sum \bar{p}^\alpha \mathbf{I} \quad (9)$$

where the first component  $\bar{\sigma}_s = (\bar{\sigma}_{ss} + \bar{\sigma}_{se})$  is the total contribution due to the solid skeleton and erodible fines, while the second component  $\sum \bar{p}^\alpha = (n_w p_f + n_{sf} p_f + n_a p_a)$  is the total contribution due to pore fluids, neglecting the compressibility of solid grains. By substituting the partial stress into Eq. (9) and rearranging the resulting equation, the following total stress equation for the soil mixture can be obtained [60–63,66]:

$$\sigma = \sigma' - [S_r p_f + (1 - S_r) p_a] \mathbf{I} \quad (10)$$

with the effective stress tensor being:

$$\boldsymbol{\sigma}' = (\boldsymbol{\sigma} + p_a \mathbf{I}) - S_r(p_a - p_f) \mathbf{I} \quad (11)$$

The above effective stress equation shares the same form as that of Eq. (7), except that the effective stress parameter  $\chi$  has been now replaced by the degree of saturation  $S_r$ , and have been commonly reported in the literature [60–63]. Because the degree of saturation is a function of suction, this form of the effective stress equation agrees well with the argument made by Khalili et al. [59], which suggested that  $\chi$  should be a function of suction. Finally, the partial stress of the solid mixture ( $ss$ ,  $se$ ) can be expressed via the effective stress as follows,

$$\bar{\boldsymbol{\sigma}}_s = \boldsymbol{\sigma}' - (1 - \phi) [S_r p_f + (1 - S_r) p_a] \mathbf{I} \quad (12)$$

It will be shown later that our proposed mathematical framework can either make use of the total stress or partial stress of the solid mixture. As a result, so long as an appropriate definition of effective stress is defined, it can be incorporated into our proposed mathematical model. In other words, our proposed mathematical model does not tie to a specific definition of effective stress.

### 2.3. Mass conservation equations

The mass conservations equation for each homogenised phase, as shown in Fig. 1(c), can be now established and subsequently used to derive essential coupled governing equations to describe the internal erosion process. For each homogenised phase in the RVE, the general mass conservation equation can be written as follows:

$$\frac{d^\alpha \bar{\rho}_\alpha}{dt} + \bar{\rho}_\alpha \nabla \cdot \mathbf{v}_\alpha = \pm \hat{\rho}_\alpha^{ex} \quad (13)$$

where  $d^\alpha \pi / dt \equiv \partial \pi / \partial t + \mathbf{v}_\alpha \cdot \nabla \pi$  denotes the material derivative of a field quantity ( $\pi$ ) on phase  $\alpha$ ; and  $\mathbf{v}_\alpha$  is the velocity vectors of phase  $\alpha$  in the mixture;  $\hat{\rho}_\alpha^{ex}$  is the mass exchange term controlled by erosion/deposition laws with a positive sign indicating mass gained, whilst a negative sign means mass loss of the corresponding phase  $\alpha$ . Here, the mass exchange is only considered to occur between the erodible-fines and fluidised-particle phases. Thus,  $\hat{\rho}_s^{ex}$  is negative when the eroded mass from the erodible-fines phase is transferred to the fluidised-particle phase. Next, by adopting the assumptions related to the velocity and compressibility of the solid and fluid phases, the mass conservation equation for each phase can be written on the material reference system of the solid skeleton ( $ss$ ) phase as follows:

$$\frac{d^{ss}[(1 - f_c)(1 - \phi)\rho_s]}{dt} + (1 - f_c)(1 - \phi)\rho_s \nabla \cdot \mathbf{v}_s = 0 \quad (14)$$

$$\frac{d^{ss}[f_c(1 - \phi)\rho_s]}{dt} + f_c(1 - \phi)\rho_s \nabla \cdot \mathbf{v}_s = -\hat{\rho}_s^{ex} \quad (15)$$

$$\frac{d^{ss}[(1 - C)S_r\phi\rho_w]}{dt} + (\mathbf{v}_f - \mathbf{v}_s) \cdot \nabla[(1 - C)S_r\phi\rho_w] + (1 - C)S_r\phi\rho_w \nabla \cdot \mathbf{v}_f = 0 \quad (16)$$

$$\frac{d^{ss}(CS_r\phi\rho_s)}{dt} + (\mathbf{v}_f - \mathbf{v}_s) \cdot \nabla(CS_r\phi\rho_s) + CS_r\phi\rho_s \nabla \cdot \mathbf{v}_f = \hat{\rho}_s^{ex} \quad (17)$$

$$\frac{d^{ss}[(1 - S_r)\phi\rho_a]}{dt} + (\mathbf{v}_a - \mathbf{v}_s) \cdot \nabla[(1 - S_r)\phi\rho_a] + (1 - S_r)\phi\rho_a \nabla \cdot \mathbf{v}_a = 0 \quad (18)$$

The above mass conservation equations for each phase in the five-phase system can be used to establish essential equations, which can be numerically solved to describe the behaviour of the five-phase system. For instance, the combination of Eqs. (14) & (15) leads to the following equation to describe the change of porosity in the five-phase system or the mass conservation equation for the solid mixture:

$$\frac{d^{ss}\phi}{dt} = (1 - \phi) \nabla \cdot \mathbf{v}_s + \hat{n}_s^{ex} \quad (19)$$

where  $\hat{n}_s^{ex} = \hat{\rho}_s^{ex}/\rho_s$  is the exchange of volume fraction due to internal erosion.

The variation of fines content caused by internal erosion can be then obtained by combining Eqs. (15) & (19), leading to:

$$\frac{d^{ss}f_c}{dt} = \frac{f_c - 1}{1 - \phi} \hat{n}_s^{ex} \quad (20)$$

Next, the mass conservation equation for the fluid mixture ( $s_f, w$ ) is required to describe the evolution of solid concentration in the fluid mixture. This can be achieved by combining Eqs. (16) & (17), taking into consideration the definition of  $\rho_f$  in Eq. (4), giving:

$$\frac{S_r \phi}{\rho_f} \frac{d^{ss} \rho_f}{dt} + \frac{d^{ss} (S_r \phi)}{dt} + (\mathbf{v}_f - \mathbf{v}_s) \nabla \cdot (S_r \phi) + S_r \phi \nabla \cdot \mathbf{v}_f = \hat{\rho}_s^{ex} / \rho_f \quad (21)$$

By combining Eqs. (17) and (21), the following equation can be derived for the rate of change of concentration:

$$\frac{d^{ss} C}{dt} + (\mathbf{v}_f - \mathbf{v}_s) \nabla \cdot C - \frac{C}{\rho_f} \frac{d^{ss} \rho_f}{dt} = \hat{n}_s^{ex} (1 - C \frac{\rho_s}{\rho_f}) / S_r \phi \quad (22)$$

The rate of change of fluid mixture density can be estimated by enforcing the following linear relationship with the rate of change of the pore-fluid pressure [50,67]:

$$\frac{1}{\rho_f} \frac{d^{ss} \rho_f}{dt} = - \frac{1}{V_f} \frac{d^{ss} V_f}{dt} = - \frac{d^{ss} \epsilon_f}{dt} = \frac{1}{K_f} \frac{d^{ss} p_f}{dt} \quad (23)$$

where  $V_f$ ,  $p_f$ , and  $K_f$  denote the volume, pressure, and bulk modulus of the fluid mixture, respectively. By substituting Eq. (23) into Eq. (22), the following equation can be obtained:

$$\frac{d^{ss} C}{dt} + (\mathbf{v}_f - \mathbf{v}_s) \nabla C - \frac{C}{K_f} \frac{d^{ss} p_f}{dt} = \hat{n}_s^{ex} (1 - C \frac{\rho_s}{\rho_f}) / S_r \phi \quad (24)$$

The above equation can be used to describe the evolution of solid concentration in the fluid mixture caused by internal erosion and transport of fluidised solid particles, in which the variation of the pore-fluid pressure can be obtained by solving the fluid mixture flow equation. In practice, the contribution of the rate of change of pore-fluid pressure (i.e., the third term on the left-hand side of Eq. (24)) has negligible influence on the concentration rate and thus can be neglected. By adopting this assumption, the concentration equation (24) can be simplified as follows:

$$\frac{d^{ss} C}{dt} + (\mathbf{v}_f - \mathbf{v}_s) \nabla C = \hat{n}_s^{ex} (1 - C \frac{\rho_s}{\rho_f}) / S_r \phi \quad (25)$$

To close the above equation, the relative velocity between solid and fluid mixtures is required, and this can be obtained from the momentum conservation equations of the mixtures, which will be derived in the next section.

## 2.4. Momentum conservation equations

The momentum conservation equations for each phase in the RVE can be expressed as:

$$\bar{\rho}_\alpha \frac{d^\alpha \mathbf{v}_\alpha}{dt} = \nabla \cdot \bar{\sigma}_\alpha + \bar{\rho}_\alpha \mathbf{b} + \sum \mathbf{Y}^{\alpha\beta} \quad (26)$$

where  $\mathbf{v}_\alpha$  is the velocity vector;  $\bar{\sigma}_\alpha$  is the partial stress tensor;  $\mathbf{b}$  is the body force vector; and  $\mathbf{Y}^{\alpha\beta}$  is the total interaction force between phases  $\alpha$  and  $\beta$ . Here, we have ignored the density-driven momentum production due to internal erosion, which will be considered in future works.

The interaction between fluid (or air) and solid phases in a porous medium can be described using the following viscous drag force equation [68]:

$$\mathbf{R}^{f,s} = - \frac{\bar{\rho}_f \mathbf{g}}{k_f} n_f (\mathbf{v}_f - \mathbf{v}_s) + p_f \nabla n_f \quad (27)$$

where  $k_f$  is the coefficient of permeability;  $\bar{\rho}_f$  is the partial density of the fluid phase;  $p_f$  is the pore-fluid pressure;  $(\mathbf{v}_f - \mathbf{v}_s)$  is the relative velocity between fluid and solid phases; and  $n_f$  is the volume fraction of the fluid phase. The last term in Eq. (27) represents the buoyancy force acting on the solid phase. In the current mathematical model, the above viscous drag force represents the interaction between solid (i.e., solid skeleton and erodible fines) and fluid (i.e., water and fluidised solid phases) mixtures or the air phase. Accordingly, the viscous drag force between each pair of continuum fluid and solid phases in the five-phase system should be proportional to its void fraction in such a way that the total viscous drag force in the five-phase system holds for Eq. (27). For this reason, the

viscous drag force between each pair of continuum fluid and solid phases can be redefined as follows:

$$\mathbf{R}^{\alpha,\beta} = \frac{n_\alpha n_\beta}{n_f n_s} \left[ -\frac{\bar{\rho}_f g}{k_f} n_f (\mathbf{v}_f - \mathbf{v}_s) + p_f \nabla n_f \right] \quad (28)$$

where  $\alpha$  and  $\beta$  indicate the individual continuum fluid and solid phases in the five-phase system, respectively. Eq. (28) can be equally adopted to describe the interaction between the air phase and the solid mixture by replacing fluid quantities with those of the air phase.

On the other hand, the interaction between water and air phases can be neglected. The interaction between the solid skeleton and erodible-fines phases can be described by an appropriate interaction law, which takes a general form of  $\mathbf{F}^{ss,se} = -\mathbf{F}^{se,ss}$ . Similarly, the interaction between fluidised particles and water phases can also be described by an appropriate law such that  $\mathbf{D}^{w,sf} = -\mathbf{D}^{sf,w}$ . By adopting these assumptions, the momentum balance equation for each phase in the five-phase system can be simplified:

$$\bar{\rho}_{ss} \frac{d^{ss}\mathbf{v}_{ss}}{dt} = \nabla \cdot \bar{\sigma}_{ss} + \bar{\rho}_{ss} \mathbf{b} + \mathbf{R}^{ss,w} + \mathbf{R}^{ss,sf} + \mathbf{R}^{ss,a} + \mathbf{F}^{ss,se} \quad (29)$$

$$\bar{\rho}_{se} \frac{d^{se}\mathbf{v}_{se}}{dt} = \nabla \cdot \bar{\sigma}_{se} + \bar{\rho}_{se} \mathbf{b} + \mathbf{R}^{se,w} + \mathbf{R}^{se,sf} + \mathbf{R}^{se,a} + \mathbf{F}^{se,ss} \quad (30)$$

$$\bar{\rho}_w \frac{d^w\mathbf{v}_w}{dt} = \nabla \cdot \bar{\sigma}_w + \bar{\rho}_w \mathbf{b} + \mathbf{R}^{w,ss} + \mathbf{R}^{w,se} + \mathbf{D}^{w,sf} \quad (31)$$

$$\bar{\rho}_{sf} \frac{d^{sf}\mathbf{v}_{sf}}{dt} = \nabla \cdot \bar{\sigma}_{sf} + \bar{\rho}_{sf} \mathbf{b} + \mathbf{R}^{sf,ss} + \mathbf{R}^{sf,se} + \mathbf{D}^{sf,w} \quad (32)$$

$$\bar{\rho}_a \frac{d^a\mathbf{v}_a}{dt} = \nabla \cdot \bar{\sigma}_a + \bar{\rho}_a \mathbf{b} + \mathbf{R}^{a,ss} + \mathbf{R}^{a,se} \quad (33)$$

Converting the above momentum equations to the same material derivative framework of the solid skeleton phase ( $ss$ ) and assuming that the relative accelerations of the water/air phases to the solid skeleton phase ( $\dot{\mathbf{v}}_{f/a} - \dot{\mathbf{v}}_{ss}$ ) are much smaller than the acceleration of the solid skeleton phase ( $\dot{\mathbf{v}}_{ss}$ ) [50,69], the following momentum equation for the entire five-phase mixture can be derived by summing all the above momentum equations of each phase, and after ignoring diffusive terms [50,69], giving:

$$\rho_t \frac{d^{ss}\mathbf{v}_s}{dt} = \nabla \cdot \sigma + \rho_t \mathbf{b} \quad (34)$$

On the other hand, the momentum equation for the solid mixture (i.e.,  $ss$  and  $se$ ) can be derived by combining Eq. (29) & (30), giving:

$$\bar{\rho}_s \frac{d^{ss}\mathbf{v}_s}{dt} = \nabla \cdot \bar{\sigma}_s + \bar{\rho}_s \mathbf{b} + \mathbf{R}^{s,f} \quad (35)$$

By substituting  $\bar{\sigma}_s$  and  $\mathbf{R}^{s,f}$  into Eq. (35), we can get:

$$\bar{\rho}_s \frac{d^{ss}\mathbf{v}_s}{dt} = \nabla \cdot [\sigma' - (1 - \phi) S_r p_f] + \bar{\rho}_s \mathbf{b} + \frac{\bar{\rho}_f g}{k_f} n_f (\mathbf{v}_f - \mathbf{v}_s) - p_f \nabla n_f \quad (36)$$

Eq. (34) can be numerically solved to describe the motion of the solid phase in the five-phase mixture once the effective stress and the pore-fluid pressure are defined. Alternatively, Eq. (36) can be equally chosen to describe the motion of the solid mixture, and in this way, the influence of seepage force is considered. The inclusion of seepage force in the momentum equation enables the proposed mathematical model to describe better the piping phenomenon caused by seepage erosion.

To close the above momentum equations, one needs to define the effective stress and the fluid pressure. The former can be computed by adopting an appropriate constitutive model, which will be discussed later, whilst the latter requires establishing flow equations to govern the evolution of air and fluid pressures in the mixture. Darcy laws for the fluid mixture and the air phase are required to establish such flow equations. For the fluid mixture, the following momentum equation can be derived:

$$\bar{\rho}_f \frac{d^{ss}\mathbf{v}_f}{dt} = \nabla \cdot \bar{\sigma}_f + \bar{\rho}_f \mathbf{b} + \mathbf{R}^{f,s} \quad (37)$$

where  $\bar{\rho}_f$  and  $\bar{\sigma}_f$  are the density and partial stress of the fluid mixture, respectively;  $\mathbf{R}^{f,s}$  is the sum of all drag forces between fluid and solid phases, resulting in the total interaction force between fluid and solid mixtures.

Next, by substituting the partial stress ( $\bar{\sigma}_f$ ) and interaction forces  $\mathbf{R}^{f,s}$  into Eq. (37), the following equation can be obtained:

$$\bar{\rho}_f \left[ \frac{d^{ss}\mathbf{v}_s}{dt} + \left( \frac{d^{ss}\mathbf{v}_f}{dt} - \frac{d^{ss}\mathbf{v}_s}{dt} \right) \right] = -n_f \nabla p_f + \bar{\rho}_f \mathbf{b} - \frac{\bar{\rho}_f g}{k_f} n_f (\mathbf{v}_f - \mathbf{v}_s) \quad (38)$$

where  $k_f$  is the coefficient of permeability.

By rearranging the above equation, assuming the difference between accelerations of the soil skeleton and pore fluid is sufficiently small, the relative velocities between fluid and solid mixtures can be written as:

$$\mathbf{q}_f = n_f (\mathbf{v}_f - \mathbf{v}_s) = \frac{k_f}{\rho_f g} \left( -\nabla p_f + \rho_f \mathbf{b} - \rho_f \frac{d^{ss}\mathbf{v}_s}{dt} \right) \quad (39)$$

Using the similar approach, the following relative velocities between the air phase and the solid mixture can be derived:

$$\mathbf{q}_a = n_a (\mathbf{v}_a - \mathbf{v}_s) = \frac{k_a}{\rho_a g} \left( -\nabla p_a + \rho_a \mathbf{b} - \rho_a \frac{d^{ss}\mathbf{v}_s}{dt} \right) \quad (40)$$

## 2.5. Flow equations for the fluid mixture and air phase

The general flow equations for the fluid mixture and air phase in the five-phase system can be derived by combining their mass and momentum conservation equations. Taking into consideration of the porosity change in Eq. (19), the mass conservation equation for the fluid mixture Eq. (21) and the air phase Eq. (18) can be re-written as follows, respectively:

$$\frac{S_r \phi}{\rho_f} \frac{d^{ss}\rho_f}{dt} + \phi \frac{d^{ss}S_r}{dt} + S_r \nabla \cdot \mathbf{v}_s + \nabla \cdot [S_r \phi (\mathbf{v}_f - \mathbf{v}_s)] = \left( \frac{\rho_s}{\rho_f} - S_r \right) \hat{n}_s^{ex} \quad (41)$$

$$\frac{(1 - S_r) \phi}{\rho_a} \frac{d^{ss}\rho_a}{dt} - \phi \frac{d^{ss}S_r}{dt} + (1 - S_r) \nabla \cdot \mathbf{v}_s + \nabla \cdot [(1 - S_r) \phi (\mathbf{v}_a - \mathbf{v}_s)] = (S_r - 1) \hat{n}_s^{ex} \quad (42)$$

The rate of change of fluid mixture ( $\rho_f$ ) and air ( $\rho_a$ ) densities can be related to their pore-pressure using their state equations. For the fluid mixture, Eq. (23) can be used, whilst for the air phase, the following equation for perfect gas can be adopted [67,69]:

$$\frac{d^{ss}\rho_a}{dt} = \frac{M_a}{RT} \frac{d^{ss}p_a}{dt} \quad (43)$$

where  $M_a$  is the molar mass of the gas phase;  $R$  is the universal gas constant; and  $T$  is the common absolute temperature. It is noted here that moist air in the pore system normally consists of two ideal gases (i.e., dry air and water vapour), whose pressure follows the same equation for a perfect gas and the total air pressure is the sum of pressure from each gas component. Here, for the sake of simplicity, we consider moist air as general gas.

By substituting the state equations for the fluid and air phases to Eqs. (41) & (42) and making use of the relative velocity between the fluid and solid mixtures, as well as between the solid mixture and air phase, established in Eqs. (39) & (40), the following general flow equations for fluid mixture and air can be derived, respectively:

$$\left( \frac{S_r \phi}{K_f} + \phi \frac{d^{ss}S_r}{d^{ss}p_f} \right) \frac{d^{ss}p_f}{dt} + S_r \nabla \cdot \mathbf{v}_s + \nabla \cdot \left[ \frac{k_f}{\rho_f g} \left( -\nabla p_f + \rho_f \mathbf{b} - \rho_f \frac{d^{ss}\mathbf{v}_s}{dt} \right) \right] = \left( \frac{\rho_s}{\rho_f} - S_r \right) \hat{n}_s^{ex} \quad (44)$$

$$\begin{aligned} \left( \frac{M_a (1 - S_r) \phi}{RT} - \phi \frac{d^{ss}S_r}{d^{ss}p_a} \right) \frac{d^{ss}p_a}{dt} + (1 - S_r) \nabla \cdot \mathbf{v}_s \\ + \nabla \cdot \left[ \frac{k_a}{\rho_a g} \left( -\nabla p_a + \rho_a \mathbf{b} - \rho_a \frac{d^{ss}\mathbf{v}_s}{dt} \right) \right] = (S_r - 1) \hat{n}_s^{ex} \end{aligned} \quad (45)$$

Given a suitable hydraulic constitutive relation, the above equations can be numerically solved for the evolution of pore-fluid and pore-air in the multi-phase mixture. In this study, a simplified version of the above flow equations is considered to establish the first SPH framework to study internal erosion through deformable porous media under complex boundary conditions. In particular, in the remainder of this paper, the pore-air pressure will be assumed to be zero ( $p_a = 0$ ). By neglecting the evolution of the pore-air pressure, Eq. (45) can be disregarded, and the suction ( $p_s = p_a - p_f$ ) will be equal to the negative pore-fluid pressure.

The above equation can be numerically solved for the evolution of the pore-fluid in the five-phase system once a suitable hydraulic model and erosion law are adopted. In practice, it is more convenient to convert the above equation into the pressure head equation. This can be achieved by making use of the following definitions of the fluid-pressure head ( $h = p_f/\gamma_f$ ) and total fluid-pressure head ( $H = h + z$ ), with  $z$  being the elevation, and after neglecting the spatial variation of fluid density, leading to:

$$\frac{d^{ss}h}{dt} = \frac{1}{C_r} \left\{ -S_r \nabla \cdot \mathbf{v}_s + \nabla \cdot \left[ k_f \left( \nabla H + \frac{1}{g} \frac{d^{ss}\mathbf{v}_s}{dt} \right) \right] + \left( \frac{\rho_s}{\rho_f} - S_r \right) \hat{n}_s^{ex} \right\} \quad (46)$$

where  $C_r = \left[ \frac{S_r \phi \gamma_f}{K_f} + \phi \frac{d^{ss}S_r}{dh} \right]$  is the storage coefficient, in which  $d^{ss}S_r/dh$  is the specific moisture term, which can be computed from a suitable hydraulic constitutive model to be described in the next section.

## 2.6. Hydraulic constitutive model

A hydraulic constitutive model or soil–water characteristic curve (SWCC) is required to solve Eq. (46) to describe the unsaturated seepage flows in the five-phase system. Among various SWCCs available in the literature, the van-Genuchten model [70] is adopted in this study. This model makes use of three parameters to relate the variation of the degree of saturation ( $S_r$ ) to that of suction head ( $-h$ ) as follows:

$$S_r = S_{res} + (S_{sat} - S_{res}) [1 + (g_a |h|)^{g_n}]^{g_c} \quad (47)$$

where  $S_{res}$  is the residual degree of saturation, indicating the amount of water retained in the soil even at a high suction;  $S_{sat}$  is the saturated saturation when pores are fully filled with water; and  $g_a$ ,  $g_n$  and  $g_c = (1 - g_n)/g_n$  are empirical fitting parameters, which can be used to best-fit hydraulic properties of different soils.

In addition to the hydraulic model, a hydraulic conductivity model, which relates the coefficient of permeability to the degree of saturation, is required. Here, the Mualem–Van Genuchten is adopted and taken the following form:

$$k = k_{sat}(\phi) S_e^{g_l} \left[ 1 - \left( 1 - S_e^{\frac{g_n}{g_n-1}} \right)^{\frac{g_n-1}{g_n}} \right]^2 \quad (48)$$

where  $S_e = \frac{S_r - S_{res}}{S_{sat} - S_{res}}$  is the effective saturation;  $k_{sat}(\phi)$  is the saturated water permeability, which can be linked to the variation of porosity using the well-known Kozeny–Carman equation [71,72]:

$$k_{sat}(\phi) = k_{sat0} \frac{(1 - \phi_0)^2}{\phi_0^3} \frac{\phi^3}{(1 - \phi)^2} \quad (49)$$

where  $\phi$  is the current porosity;  $\phi_0$  is the initial porosity; and  $k_{sat0}$  is the initial saturated permeability coefficient value determined from laboratory tests.

## 2.7. Erosion and deposition laws

Mass or volume exchange laws are required to complete the proposed five-phase erosion mathematical model. In this study, the following volume exchange ( $n_s^{ex}$ ), which considers both erosion and deposition caused by the migration of fine particles into and out of the RVE, is adopted [18]:

$$\hat{n}_s^{ex} = \hat{n}_e + \hat{n}_d \quad (50)$$

where  $\hat{n}_e$  and  $\hat{n}_d$  are erosion and deposition rates, respectively.

Several empirical equations describing erosion and deposition rate were proposed in the literature, most of which are linked to the variations of porosity, fines content/concentration, ultimate fines content and flow characteristics (i.e. seepage velocity or hydraulic gradient). Table 1 summarises common erosion/deposition laws [20,73–75]. The predictive capability of these erosion/deposition laws in the current five-phase model will be investigated later in Section 4. Finally, to complete the proposed governing equations for coupled seepage-erosion and flow-deformation in unsaturated/saturated porous media, a robust constitutive model capable of describing the influence of suction and mass loss on the overall shear strength of soils is required, and this will be discussed in the next section.

**Table 1**

Summary of erosion/deposition laws.

Erosion laws	References	Deposition laws	References
$\hat{n}_e = \begin{cases} \lambda_e (f_c - f_{c\infty})  \mathbf{q}_f  & (f_c > f_{c\infty}) \\ 0 & (f_c < f_{c\infty}) \end{cases}$			
1 $f_{c\infty} = \begin{cases} f_{c0} - (f_{c0} - f_{c\infty}^*) \frac{ \mathbf{q}_f }{ \mathbf{q}_f^* } & 0 \leq  \mathbf{q}_f  \leq  \mathbf{q}_f^*  \\ f_{c\infty}^* - \alpha_{er} \log \left( \frac{ \mathbf{q}_f }{ \mathbf{q}_f^* } \right) &  \mathbf{q}_f  \geq  \mathbf{q}_f^*  \end{cases}$	Cividini & Gioda [76]	1 $\hat{n}_d = \lambda_d C  \mathbf{q}_f $	Schaufler et al. [77]
2 $\hat{n}_e = \lambda_e (1 - \phi) (f_c - f_{c\infty})  \mathbf{q}_f $ $f_{c\infty} = f_{c0} \cdot \exp(-t^b i^c / a)$ or $f_{c\infty} = f_{c0} \cdot [(1 - c) \cdot \exp(-a \cdot t^b) + d]$	Yang et al. [20,73] Sterpi [74] Cividini et al. [75]	2 $\hat{n}_d = \lambda_d (1 - \phi) C  \mathbf{q}_f $	Vardoulakis et al. [13]
3 $\hat{n}_e = \lambda_e f_c  \mathbf{q}_f $	Khalil et al. [78]	3 $\hat{n}_d = \lambda_d (1 - \phi) C  \mathbf{q}_f ^2$	Steeb et al. [15]

## 2.8. A simple suction/erosion-dependent constitutive model

The internal erosion process caused by seepage flows mostly occurs in fully saturated soils. However, to properly describe this process at the field scale suitable for general boundary value applications (e.g., predictions of dam/embankment failures due to internal erosion), which normally involve both saturated and unsaturated soils, it is crucial to consider the influence of suction on the shear strength of soils, in addition to its influence due to mass loss. In this work, to account for the influences of suction and/or erosion on the shear strength of soils, a simple suction/erosion-dependent constitutive model is proposed. First, the shear strength of soils, represented by friction ( $\varphi$ ) and cohesion ( $c$ ), is divided into the effective and suction-dependent parts:

$$\varphi = \varphi' + \varphi_s \quad (51)$$

$$c = c' + c_s \quad (52)$$

where  $\varphi'$  and  $c'$  represent the friction and apparent cohesion of the soil at its fully saturated condition, whilst  $\varphi_s$  and  $c_s$  indicate the additional shear strength due to suction.

The suction-dependent friction and cohesion strengths can be defined as [79]:

$$\varphi_s = \phi_{s0} \left( \frac{p_s}{p_{atm}} \right) \quad (53)$$

$$c_s = c_{s0} \left[ 1 - e^{-B_s \left( \frac{p_s}{p_{atm}} \right)} \right] \quad (54)$$

where  $\phi_{s0}$  and  $c_{s0}$  are the maximum increases of friction angle and cohesion caused by suction;  $p_s$  is the suction;  $p_{atm}$  is the atmospheric pressure, which is equals to 101 kpa; and  $B_s$  is a constant controlling the rate of variation of apparent cohesion with suction. The above suction-dependent strength model suggests that the shear strength of unsaturated soils gradually reduces to their saturated strength as the degree of saturation increases or  $p_s$  reduces to zero as the fully saturated condition is reached.

In addition, it is commonly reported from triaxial or shear experiments that the effective shear strength of soils (e.g., over-consolidated clays or medium/dense sands) gradually reduces to reach their residual or critical state strength at large shear deformation. To account for this softening behaviour, the effective friction angle and cohesion strength can be modelled as an exponential function of the accumulated equivalent plastic shear strain [80,81]:

$$\varphi' = \varphi'_{res} + (\varphi'_{peak} - \varphi'_{res}) e^{-\eta \varepsilon_p^{eq}} \quad (55)$$

$$c' = c'_{res} + (c'_{peak} - c'_{res}) e^{-\eta \varepsilon_p^{eq}} \quad (56)$$

where  $(\varphi'_{res}, c'_{res})$  and  $(\varphi'_{peak}, c'_{peak})$  are residual and peak shear strength of soils, respectively;  $\eta$  is a constant parameter, controlling the rate of soil strength degradation; and  $\varepsilon_p^{eq} = (\boldsymbol{\epsilon}_p : \boldsymbol{\epsilon}_p)^{0.5}$  is the accumulated plastic shear strain with  $\boldsymbol{\epsilon}_p$  being the deviatoric plastic strain tensor.

Finally, to consider the effect of mass loss caused by internal erosion on the shear strength of soils, this study assumes that the effective peak shear strength of soils (i.e.  $\varphi'_{peak}$  and  $c'_{peak}$ ) is dependent on the erosion rate or the erodible fines content of soils. This assumption reflects the commonly reported experimental and numerical observations on the influence of internal erosion on the shear strength of soils, in which the peak shear strength of soils is reported to reduce with increasing internal erosion rate until reaching their residual or critical shear strengths [82,83]. On the other hand, it is reasonable to consider that internal erosion produces negligible influence on the residual shear strength of soils compared to its influence on the peak shear strength [82,83]. In this work, the influence of erosion on the peak effective shear strength of soils is formulated as follows:

$$\varphi'_{peak} = \varphi'_{res} + (\varphi'_{pk0} - \varphi'_{res}) \left( \frac{f_c - f_{c\infty}}{f_{c0} - f_{c\infty}} \right) \quad (57)$$

$$c'_{peak} = c'_{res} + (c'_{pk0} - c'_{res}) \left( \frac{f_c - f_{c\infty}}{f_{c0} - f_{c\infty}} \right) \quad (58)$$

where  $(\varphi'_{pk0}, c'_{pk0})$  are initial values of the peak effective friction angle and cohesion;  $(\varphi'_{res}, c'_{res})$  are residual friction angle and cohesion strength at the ultimate fines content ( $f_{c\infty}$ ), which is the ultimate state at which no further erosion would occur;  $f_{c0}$  is the initial fines content; and  $f_c$  is the fines content at the current state.

A yield function is now required to describe the inelastic response of the materials, and in this work, the general form of the Drucker–Prager yield function is extended to incorporate the effects of suction and erosion on the shear strength of soils. The general suction/erosion-dependent Drucker–Prager yield surface takes the following form:

$$y(\sigma, \varepsilon_p^{eq}, p_s, f_c) = \sqrt{J_2} + \alpha_\varphi(\varepsilon_p^{eq}, p_s, f_c) I_1 - k_c(\varepsilon_p^{eq}, p_s, f_c) = 0 \quad (59)$$

where  $I_1$  and  $J_2$  are the first and second invariants of the stress tensor;  $\alpha_\varphi(\varepsilon_p^{eq}, p_s, f_c)$  and  $k_c(\varepsilon_p^{eq}, p_s, f_c)$  are the shear strength parameters related to the total friction angle ( $\varphi$ ) and cohesion ( $c$ ), respectively. These parameters in the plane strain condition are defined as follows:

$$\begin{aligned} \alpha_\varphi(\varepsilon_p^{eq}, p_s, f_c) &= \frac{\tan \varphi(\varepsilon_p^{eq}, p_s, f_c)}{\sqrt{9 + 12 \tan^2 \varphi(\varepsilon_p^{eq}, p_s, f_c)}} \\ k_c(\varepsilon_p^{eq}, p_s, f_c) &= \frac{3c\varphi(\varepsilon_p^{eq}, p_s, f_c)}{\sqrt{9 + 12 \tan^2 \varphi(\varepsilon_p^{eq}, p_s, f_c)}} \end{aligned} \quad (60)$$

On the other hand, a potential plastic function (or dilatancy rule) is required to describe the direction of plastic strain development. In this work, the following plastic potential function is adopted:

$$g(\sigma, \psi) = \alpha_\psi I_1 + \sqrt{J_2} \quad (61)$$

where  $\alpha_\psi$  is a parameter dependent on dilatancy angle  $\psi$  and shares the same formulation as that of  $\alpha_\varphi$  in which  $\varphi$  is replaced  $\psi$ . Triaxial experimental evidence suggests that the dilatancy angle reduces to zero as the soil reaches its critical state with no further volume change. Furthermore, as the soil reaches its critical state, it undergoes significant plastic shear deformation. By making use of these observations, the dilatancy angle can be related to the accumulated plastic shear strain as follows [84]:

$$\psi = \psi_0 e^{-\alpha \varepsilon_p^{eq}} \quad (62)$$

where  $\psi_0$  is the initial dilatancy angle before shearing, and  $\alpha$  is a fitting parameter that can be calibrated with sufficient experimental data or using an optimisation method [85,86]. It is worth noting that internal erosion also modifies the dilation–contraction behaviour of the soil, and such complex responses require more advanced dilatancy laws or advanced constitutive models [87,88], which are beyond the scope of this paper.

The general stress–strain relation can be now derived following the standard plasticity framework with all the above components. The effective stress increment ( $d\sigma'$ ) can be defined from the generalised Hooke's law:

$$d\sigma' = \mathbf{D}^e : (d\boldsymbol{\epsilon} - d\boldsymbol{\epsilon}_p) = \mathbf{D}^{ep} : d\boldsymbol{\epsilon} \quad (63)$$

where  $\mathbf{D}^e$  and  $\mathbf{D}^{ep}$  are the elastic and elastoplastic stiffness moduli;  $d\boldsymbol{\epsilon}$  is the total strain increment and  $d\boldsymbol{\epsilon}_p$  is the plastic strain increment, which can be defined as follows:

$$d\boldsymbol{\epsilon}_p = d\lambda \frac{\partial g(\sigma', \psi)}{\partial \sigma'} \quad (64)$$

**Table 2**

Semi-implicit stress updating algorithm.

---

**1** Given incremental strain and rotation tensors ( $d\boldsymbol{\epsilon}$ & $d\boldsymbol{\omega}$ ) and other state variables at  $t$ , evaluate elastic trial stress for plastic loading:

$$\text{Elastic trial stress increment: } d\boldsymbol{\sigma}_{t+1}^{eir} = \mathbf{D}^e : d\boldsymbol{\epsilon} - d\boldsymbol{\omega} \cdot \boldsymbol{\sigma}'_t + \boldsymbol{\sigma}'_t \cdot d\boldsymbol{\omega}$$

$$\text{Trial stress: } \boldsymbol{\sigma}_{t+1}^{tr} = \boldsymbol{\sigma}'_t + d\boldsymbol{\sigma}_{t+1}^{eir}$$

$$\text{Trial yield function: } y_{t+1}^{tr}(\boldsymbol{\sigma}_{t+1}^{tr}, \boldsymbol{\varepsilon}_{p_t}^{eq}, p_{s_t}, f_{c_t})$$

---

**2** Check if plastic yielding occurs by computing:  $y_{t+1}^{tr}(\boldsymbol{\sigma}_{t+1}^{tr}, \boldsymbol{\varepsilon}_{p_t}^{eq}, p_{p_t}, f_{c_t})$

$$\text{If } y_{t+1}^{tr}(\boldsymbol{\sigma}_{t+1}^{tr}, \boldsymbol{\varepsilon}_{p_t}^{eq}, p_{s_t}, f_{c_t}) < 0 \text{ then}$$

Proceed to Step 3

$$\text{Else } y_{t+1}^{tr}(\boldsymbol{\sigma}_{t+1}^{tr}, \boldsymbol{\varepsilon}_{p_t}^{eq}, p_{s_t}, f_{c_t}) \geq 0 \text{ the loading step is elasto-plastic}$$

Proceed to Step 4

End

---

**3** Elastic stress update:

$$\boldsymbol{\sigma}'_{t+1} = \boldsymbol{\sigma}_{t+1}^{tr} \quad \boldsymbol{\varepsilon}_{t+1}^p = \boldsymbol{\varepsilon}_t^p$$

$$\boldsymbol{\varepsilon}_{p_{t+1}}^{eq} = \boldsymbol{\varepsilon}_{p_t}^{eq} \quad f_{c_{t+1}} = f_{c_t} \quad p_{s_{t+1}} = p_{s_t}$$


---

**4** Perform stress corrector:

$$d\lambda = \frac{y_{t+1}^{tr} + \frac{\partial y^{tr}}{\partial p_s} dp_s + \frac{\partial y^{tr}}{\partial f_c} df_c}{\frac{\partial y^{tr}}{\partial \boldsymbol{\sigma}'} : \mathbf{D}^e : \frac{\partial g^{tr}}{\partial \boldsymbol{\sigma}'} - \frac{\partial y^{tr}}{\partial \boldsymbol{\varepsilon}_p^{eq}} \sqrt{\frac{2}{3}} \frac{\partial g^{tr}}{\partial \boldsymbol{\sigma}'} : \frac{\partial g^{tr}}{\partial \boldsymbol{\sigma}'}}$$

$$d\boldsymbol{\sigma}'_{t+1} = \boldsymbol{\sigma}_{t+1}^{tr} - d\boldsymbol{\sigma}'^p = \boldsymbol{\sigma}'_{t+1} - d\lambda \frac{\partial g^{tr}}{\partial \boldsymbol{\sigma}'}$$

$$\boldsymbol{\sigma}'_{t+1} = \boldsymbol{\sigma}'_t + d\boldsymbol{\sigma}'_{t+1} \quad \boldsymbol{\varepsilon}_{t+1}^p = \boldsymbol{\varepsilon}_t^p + d\boldsymbol{\varepsilon}^p$$

$$\boldsymbol{\varepsilon}_{p_{t+1}}^{eq} = \boldsymbol{\varepsilon}_{p_t}^{eq} + d\boldsymbol{\varepsilon}_p^{eq} \quad f_{c_{t+1}} = f_{c_t} + df_c \quad p_{s_{t+1}} = p_s + dp_s$$

---

EXIT the algorithm

For large deformation simulations, an invariant stress increment with respect to the rigid-body rotation is required, and in this work, the Jaumann stress rate of Cauchy stress is adopted, which modifies Eq. (63) as follows:

$$d\boldsymbol{\sigma}' = \mathbf{D}^{ep} : d\boldsymbol{\epsilon} - d\boldsymbol{\omega} \cdot \boldsymbol{\sigma}' + \boldsymbol{\sigma}' \cdot d\boldsymbol{\omega} \quad (65)$$

where the  $d\boldsymbol{\omega}$  is to the incremental rotation tensor. An alternative to using the Jaumann stress rate is to adopt the finite elastoplasticity theory, and interested readers can follow the standard approach described in Neto et al. [89]. In SPH, given that the time increment is often very small, the use of the Jaumann stress rate is sufficient. The above stress-strain relation is updated using the semi-implicit stress return mapping algorithm [90–92], which has been previously demonstrated to work well within the context of SPH [41,42,93] or FEM with relatively small strain increment [94,95] is adopted. The details of this algorithm are presented in Table 2. Finally, it is worth noting that several advanced constitutive models [87,88,96–98] are available in the literature and can be straightforwardly incorporated into the current SPH framework instead of using the current simple suction/erosion-dependent model. The shortcoming of these advanced models is that they often consist of a large number of material constitutive parameters, some of which are difficult to calibrate and thus limit them from practical applications.

The proposed mathematical framework for describing the fully coupled behaviour of seepage-induced internal erosion and failure in saturated/unsaturated porous media is summarised in Table 3. These governing equations are written as partial differential equations (PDEs). The basic unknowns are porosity ( $\phi$ ), concentration ( $C$ ), fine

**Table 3**

Summary of governing equations.

Rules	Mathematical expressions	Equation No.
Evolution of porosity	$\frac{d^{ss}\phi}{dt} = (1 - \phi) \nabla \cdot \mathbf{v}_s + \hat{n}_s^{ex}$	(19)
Evolution of fines content	$\frac{d^{ss}f_c}{dt} = \frac{f_c - 1}{1 - \phi} \hat{n}_s^{ex}$	(20)
Evolution of concentration	$\frac{d^{ss}C}{dt} + (\mathbf{v}_f - \mathbf{v}_s) \nabla \cdot C = \hat{n}_s^{ex} (1 - C \frac{\rho_s}{\rho_f}) / S_r \phi$	(25)
Momentum balance of the entire mixture	$\rho_t \frac{d^{ss}\mathbf{v}_s}{dt} = \nabla \cdot \boldsymbol{\sigma} + \rho_t \mathbf{b}$	(34)
Momentum balance of the solid mixture	$\bar{\rho}_s \frac{d^{ss}\mathbf{v}_s}{dt} = \nabla \cdot \bar{\boldsymbol{\sigma}}_s + \bar{\rho}_s \mathbf{b} + \frac{\bar{\rho}_f g}{k_f} n_f (\mathbf{v}_f - \mathbf{v}_s) - p_f \nabla n_f$	(36)
Darcy's law	$\mathbf{q}_w = \frac{k_f}{\rho_f g} \left( -\nabla p_f + \rho_f \mathbf{b} - \rho_f \frac{d^{ss}\mathbf{v}_s}{dt} \right)$	(39)
Evolution of pore-fluid pressure head	$\frac{d^{ss}h}{dt} = \frac{1}{C_r} \left\{ -S_r \nabla \cdot \mathbf{v}_s + \nabla \cdot \left[ k_f \left( \nabla H + \frac{1}{g} \frac{d^{ss}\mathbf{v}_s}{dt} \right) \right] + \left( \frac{\rho_s}{\rho_f} - S_r \right) \hat{n}_s^{ex} \right\}$	(46)
Constitutive equation	$d\boldsymbol{\sigma}' = \mathbf{D}^{ep} : d\boldsymbol{\epsilon} - d\boldsymbol{\omega} \cdot \boldsymbol{\sigma}' + \boldsymbol{\sigma}' \cdot d\boldsymbol{\omega}$	(65)

content ( $f_c$ ), solid mixture velocity ( $\mathbf{v}_s$ ), Darcy's velocity  $\mathbf{q}_f$ , and fluid pressure head ( $h$ ). To solve these PDEs, one needs to convert these equations into ordinary differential equations (ODEs), which can be solved using a standard time integration scheme. SPH is selected to solve these governing equations in this paper, thanks to its capacity to handle complex multi-physics interactions and large deformation of unsaturated/saturated porous media. The details of SPH and its applications to solve the above governing equations are described in the next section.

### 3. Solution approximation using SPH

#### 3.1. The fundamentals of SPH

SPH is a Lagrangian mesh-free method in which the computational domain is discretised into numbers of material points (or particles). Each material point carries a series of information such as position, velocity, density, and stress and freely moves in the computational domain without any constraint from its neighbours. The basic SPH equations to approximate a function, its gradient and the Laplacian operator are [23,26,99–102]:

$$f(\mathbf{x}_i) = \sum_{j=1}^N V_j f(\mathbf{x}_j) W_{ij} \quad (66)$$

$$\nabla_i f(\mathbf{x}_i) = \sum_{j=1}^N V_j f(\mathbf{x}_j) \nabla_i W_{ij} \quad (67)$$

$$\nabla_i^2 f(\mathbf{x}_i) = 2 \sum_{j=1}^N V_j [f(\mathbf{x}_j) - f(\mathbf{x}_i)] \frac{\mathbf{x}_{ji} \cdot \nabla_i W_{ij}}{|\mathbf{x}_{ji}|^2} \quad (68)$$

where  $\nabla_i f(\mathbf{x}_i)$  is the first-order gradient of function  $f$ ;  $\nabla_i^2 f(\mathbf{x}_i)$  is the Laplacian operator; the subscripts  $i$  and  $j$  refer to the quantity evaluated at the position of particle  $i$  and  $j$ , respectively;  $V_j$  is the volume of particle  $j$ ;  $N$  is the total number of neighbouring particles located within the support domain of particle  $i$ ;  $\mathbf{x}_{ji}$  is the relative distance between two particles, defined by  $\mathbf{x}_{ji} = \mathbf{x}_j - \mathbf{x}_i$ ;  $W_{ij}$  and  $\nabla_i W_{ij}$  are the kernel function and its first order gradient; and  $h$  is the smoothing length defining the cut-off distance of the kernel function. In this study, the cubic spline kernel function is adopted and takes the following form:

$$W(q, h) = \alpha_d \begin{cases} \frac{2}{3} - q^2 + \frac{1}{2}q^3, & 0 \leq q < 1 \\ \frac{1}{6}(2-q)^3, & 1 \leq q < 2 \\ 0, & q \geq 2 \end{cases} \quad (69)$$

where  $\alpha_d$  is a normalised factor, which equals  $15/7\pi h^2$  for two-dimensional applications; and  $q$  is the normalised distance  $q = |\mathbf{x}_{ij}|/h$ .

Eq. (67) is commonly reported to be suffered from several inconsistency issues, which can be overcome using Taylor's expansion series. For instance, Eq. (67) can be rewritten as follow after adopting the Taylor-series to expand  $f(x_j)$  around  $x_i$ :

$$\begin{aligned}\nabla_i^n f(\mathbf{x}_i) &= \sum_{j=1}^N V_j f(\mathbf{x}_j) \nabla_i^n W_{ij} = \sum_{j=1}^N V_j [f(\mathbf{x}_i) + \nabla_i^m f(\mathbf{x}_i) (x_j - x_i)^m + O(h^2)] \nabla_i^n W_{ij} \\ &= f(\mathbf{x}_i) \sum_{j=1}^N V_j \nabla_i^n W_{ij} + \nabla_i^m f(\mathbf{x}_i) \sum_{j=1}^N \frac{m_j}{\rho_j} (x_j - x_i)^m \nabla_i^n W_{ij} + O(h^2)\end{aligned}\quad (70)$$

where superscripts  $m$  and  $n$  indicate the coordinate with repeated indexes implied summation; and  $\nabla_i^n = \partial/\partial x^n$ . It can be seen from Eq. (70) that the accuracy of SPH approximation for the first-order derivative of function  $f(\mathbf{x}_i)$  replies on how good SPH approximations to achieve  $\sum_{j=1}^N \frac{m_j}{\rho_j} \nabla_i^n W_{ij} = 0$  and  $\sum_{j=1}^N \frac{m_j}{\rho_j} (x_j - x_i)^m \nabla_i^n W_{ij} = \delta^{mn}$ , in which  $\delta^{mn}$  is the unit tensor.

In practice, the above equations are hardly achieved due to the symmetry requirement of the kernel function. As a result, Eq. (70) is suffered from low accuracy approximation for highly disordered or random particle systems. To eliminate these errors (up to 2nd accuracy of Taylor's series expansion), Eq. (70) can be rearranged, leading to the following well-known normalised SPH formulation [103,104]:

$$\nabla_i^m f(\mathbf{x}_i) = \sum_{j=1}^N V_j [f(\mathbf{x}_j) - f(\mathbf{x}_i)] \hat{\nabla}_i^m W_{ij} \quad (71)$$

where  $\hat{\nabla}_i^m W_{ij} = L_{ij}^{mn} \nabla_i^n W_{ij}$  with  $L_{ij}^{mn} = \left[ \sum_{j=1}^N \frac{m_j}{\rho_j} (x_j - x_i)^m \nabla_i^n W_{ij} \right]^{-1}$  being the renormalisation matrix. In this study, Eq. (71) is used to approximate the gradient of most physical quantities, except the gradient of stress/pressure terms in the momentum equation. This is because, for the momentum equation, it is important to ensure the conservation of linear and angular momenta. As a result, the following SPH approximation equation is adopted when it comes to approximating the gradient of stress/pressure terms in the momentum equation:

$$\nabla f(\mathbf{x}_i) = \rho_i \left[ \frac{f(\mathbf{x}_i)}{\rho_i^2} \nabla \rho_i + \nabla \left( \frac{f(\mathbf{x}_i)}{\rho_i} \right) \right] \approx \rho_i \sum_{j=1}^N m_j \left[ \frac{f(\mathbf{x}_i)}{\rho_i^2} + \frac{f(\mathbf{x}_j)}{\rho_j^2} \right] \nabla_i W_{ij} \quad (72)$$

Similar to the SPH approximation for the first-order derivative, the accuracy of the SPH approximation for the Laplacian operator can also be improved by adopting Taylor series expansion, several versions of which have been reported in the literature [26,43,101,102]. For example, Bui and Nguyen [26] proposed the following SPH approximation for the Laplacian operator:

$$\nabla_i^2 f(\mathbf{x}_i) = \frac{2}{K_{ij}} \left[ \sum_{j=1}^N V_j f_{ji} \frac{\mathbf{x}_{ji} \cdot \nabla_i W_{ij}}{|\mathbf{x}_{ji}|^2} - \sum_{j=1}^N V_j f_{ji} \hat{\nabla}_i^m W_{ij} \sum_{j=1}^N \frac{m_j}{\rho_j} \mathbf{x}_{ji}^m \frac{\mathbf{x}_{ji} \cdot \nabla_i W_{ij}}{|\mathbf{x}_{ji}|^2} \right] \quad (73)$$

where  $K_{ij} = \frac{1}{2} \left[ \sum_{j=1}^N V_j \left( x_{ji}^2 + y_{ji}^2 \right) \frac{\mathbf{x}_{ji} \cdot \nabla_i W_{ij}}{|\mathbf{x}_{ji}|^2} \right]$  and  $f_{ji} = f(\mathbf{x}_j) - f(\mathbf{x}_i)$ . It has been demonstrated that the above Laplacian operator can improve the accuracy of SPH approximation on both regular and disorder systems [26]. However, the above Laplacian SPH operator cannot be applied to problems involving anisotropic diffusion, such as the anisotropic transient seepage flow. To address this problem, Lian et al. [43] proposed a general SPH scheme for the approximation of second-order derivatives:

$$\frac{\partial^2 f_i}{\partial x^m \partial x^n} = \sum_{j=1}^N V_j (f_j - f_i) \mathcal{D}^{mn} \tilde{F}_{ij} - \frac{\partial f_i}{\partial x^{m'}} \sum_{j=1}^N V_j x_{ji}^{m'} \mathcal{D}^{mn} \tilde{F}_{ij} \quad (74)$$

where  $\mathcal{D}^{mn} = 4 \frac{x_{ji}^m x_{ji}^n}{|\mathbf{x}_{ji}|^2} - \delta^{mn}$  and  $\tilde{F}_{ij} = \frac{\mathbf{x}_{ji}}{|\mathbf{x}_{ji}|^2} \cdot \hat{\nabla}_i W_{ij}$ . In this study, given that all considered problems involve isotropic transient seepage flows in homogeneous porous media, Eq. (73) is adopted.

### 3.2. SPH approximation of governing equations

The proposed governing equations listed in [Table 3](#) for the five-phase system can be now discretised using the above SPH approximations for the first and second-order derivatives. The rate of change of porosity in Eq. [\(19\)](#) can be approximated by using Eq. [\(71\)](#), giving:

$$\left(\frac{d^{ss}\phi}{dt}\right)_i = (1 - \phi_i) \sum_{j=1}^N V_{sj} (\mathbf{v}_{sj} - \mathbf{v}_{si}) \hat{\nabla}_i W_{ij} + \hat{n}_{si}^{ex} \quad (75)$$

where  $\phi_i$  is the porosity of particle  $i$ ;  $\mathbf{v}_{si}$  and  $\mathbf{v}_{sj}$  is the velocity of soil particles  $i$  and  $j$ , respectively;  $V_{sj}$  is the volume of soil particle  $j$ ; and  $\hat{n}_{si}^{ex}$  is the volume exchange of particle  $i$ , which consists of both mass loss due to erosion and mass gained due to deposition.

The fines content in Eq. [\(20\)](#) can be solved directly without SPH approximation. The rate of change of concentration of fluidised particles in Eq. [\(25\)](#) can be approximated by using Eq. [\(71\)](#):

$$\left(\frac{d^{ss}C}{dt}\right)_i = \hat{n}_{si}^{ex} \left(1 - C_i \frac{\rho_{si}}{\rho_{fi}}\right) / (S_{ri}\phi_i) - (\mathbf{v}_{fi} - \mathbf{v}_{si}) \cdot \sum_{j=1}^N V_{sj} (C_j - C_i) \hat{\nabla}_i W_{ij} \quad (76)$$

where  $C_i$  and  $C_j$  are the concentrations at particles  $i$  and  $j$ , respectively.

The momentum balance of the solid mixture in Eq. [\(36\)](#) can be approximated by using Eq. [\(72\)](#):

$$\begin{aligned} \left(\frac{d^{ss}\mathbf{v}_s\right)_i &= \sum_{j=1}^N \bar{m}_{sj} \left( \frac{\sigma'_i - (1 - \phi_i) S_{ri} p_{fi}}{\bar{\rho}_{si}^2} + \frac{\sigma'_j - (1 - \phi_j) S_{rj} p_{fj}}{\bar{\rho}_{sj}^2} + \mathbf{C}_{ij} \right) \nabla_i W_{ij} + \mathbf{b}_i \\ &+ \frac{\bar{\rho}_{fi} g}{\bar{\rho}_{si} k_{fi}} n_{fi} (\mathbf{v}_{fi} - \mathbf{v}_{si}) - \frac{p_{fi}}{\bar{\rho}_{si}} \sum_{j=1}^N \bar{m}_{sj} (n_{fj} - n_{fi}) \hat{\nabla}_i W_{ij} \end{aligned} \quad (77)$$

where  $\bar{m}_{sj}$  is the partial mass of particle  $j$ ;  $\bar{\rho}_{si}$  and  $\bar{\rho}_{sj}$  are partial densities of particles  $i$  and  $j$ , respectively;  $\mathbf{b}_i$  is body force vector of particle  $i$ ;  $\mathbf{C}_{ij}$  is a stabilisation term used to remove stress fluctuations and tensile instability [23,52].

The hydraulic gradient of the fluid mixture and Darcy's seepage velocity in Eq. [\(39\)](#) can be approximated using Eq. [\(71\)](#), giving:

$$\nabla H_i = \sum_{j=1}^N V_{sj} (H_j - H_i) \cdot \hat{\nabla}_i W_{ij} \quad (78)$$

$$\mathbf{q}_{fi} = - \sum_{j=1}^N V_{sj} \frac{2k_{fi}k_{fj}}{k_{fi} + k_{fj}} (H_j - H_i) \cdot \hat{\nabla}_i W_{ij} - \frac{k_{fi}}{g} \frac{d^{ss}\mathbf{v}_{si}}{dt} \quad (79)$$

where  $\mathbf{q}_{fi}$  is the seepage velocity vector of particle  $i$ ;  $H$  is the total fluid pressure head; and  $k_{fi}$  is the permeability coefficient of particle  $i$ .

The rate of change of pore fluid pressure head in Eq. [\(46\)](#) can be approximated by using Eqs. [\(71\)](#) & [\(73\)](#), giving:

$$\begin{aligned} \left(\frac{d^{ss}h}{dt}\right)_i &= \left\{ \frac{2}{K_{ij}} \left[ \sum_{j=1}^N V_{sj} k_{fij} (H_j - H_i) \frac{\mathbf{x}_{ji} \cdot \nabla_i W_{ij}}{|\mathbf{x}_{ji}|^2} \right. \right. \\ &- \sum_{j=1}^N V_{sj} k_{fij} (H_j - H_i) \hat{\nabla}_i^m W_{ij} \sum_{j=1}^N V_{sj} \mathbf{x}_{ji}^m \frac{\mathbf{x}_{ji} \cdot \nabla_i W_{ij}}{|\mathbf{x}_{ji}|^2} \Big] \\ &+ \sum_{j=1}^N V_{sj} k_{fij} \frac{1}{g} \left( \frac{d\mathbf{v}_{sj}}{dt} - \frac{d\mathbf{v}_{si}}{dt} \right) \hat{\nabla}_i W_{ij} - S_{ri} \sum_{j=1}^N V_{sj} (\mathbf{v}_{sj} - \mathbf{v}_{si}) \cdot \hat{\nabla}_i W_{ij} \\ &\left. \left. + \left( \frac{\rho_{si}}{\rho_{fi}} - S_{ri} \right) \hat{n}_{si}^{ex} \right\} / C_{ri} \right\} \end{aligned} \quad (80)$$

where  $k_{fij} = 2k_{fi}k_{fj}/(k_{fi} + k_{fj})$  is the average permeability between particles  $i$  and  $j$  [102].

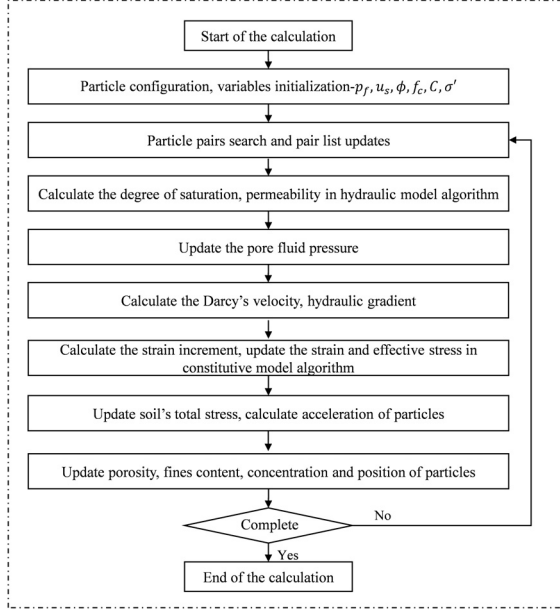


**Fig. 2.** SPH computational procedure to solving coupled governing equations.

### 3.3. Time integration and boundary conditions

[Fig. 2](#) outlines the detailed computational procedure to integrate the governing equations for the five-phase mixtures. The Leap Frog (LF) algorithm [23] is adopted to integrate field variables  $\chi$  such as pore-fluid pressure head  $h$  or soil velocity  $v_s$ . These variables are updated at the half time step as follows:

$$\chi_{n+1/2} = \chi_{n-1/2} + \Delta t \left( \frac{d\chi}{dt} \right)_n \quad (81)$$

On the other hand, the soil displacement  $x$  is updated at the full-time step:

$$\mathbf{x}_{n+1} = \mathbf{x}_n + \Delta t \mathbf{v}_{n+1/2} \quad (82)$$

The stability of the LF integration scheme is controlled by the Courant–Friedrichs–Lewy (CFL) condition. For the solid phase, the stable time step size is proportional to the smoothing length and requires the following condition:

$$\Delta t_S \leq C_{CFL}^s (h_{sml}/c_s) \quad (83)$$

where  $C_{CFL}^s$  is the Courant number for the solid phase and is taken to be 0.2;  $h_{sml}$  is smoothing length of an SPH particle; and  $c_s = \sqrt{E_s/\rho_s}$  is the sound speed.

For the fluid flow, the stable time step size requires the following conditions and the detailed derivation can be found in Lian et al. [27,43]:

$$\Delta t_F \leq \begin{cases} C_{CFL}^f \phi \left( \frac{ds_r}{dh} \right) \frac{h_{sml}^2}{k_{sat}} & (\text{unsaturated state}) \\ C_{CFL}^f \phi \frac{\gamma_f h_{sml}^2}{K_f k_{sat}} & (\text{saturated state}) \end{cases} \quad (84)$$

where  $C_{CFL}^f$  is Courant number for the fluid phase and is taken to be 0.1.

Combining the CFL conditions for the solid and fluid phases, the time step size in the simulation must satisfy the following condition:

$$\Delta t = \min(\Delta t_S, \Delta t_F) \quad (85)$$

Finally, similar to any other numerical methods, treatments of boundary conditions are required to solve boundary value problems. In this study, for the solid phases, free-slip or no-slip boundary conditions (or roller and fully

fixed boundaries) are required, and the SPH treatment for these boundary conditions was already explained in Bui et al. [23] and thus is not repeated here. Similarly, impervious boundary, constant water pressure head boundary, constant water flux boundary, and free surface boundary conditions are commonly used for the fluid phases. These boundary conditions can be either directly imposed on SPH particles located on the ground surface or through boundary particles, the treatment of which can be found in reference [27,43].

### 3.4. Stabilisation techniques

#### 3.4.1. Viscous damping for vibration and non-dissipative systems

The above SPH framework for solving the five-phase governing equations works well in most cases and achieves stable results, thanks to accurate SPH approximations for the first- and second-order derivatives. However, additional measures might be required to stabilise SPH solutions in some particular applications, such as those involving sudden applied/removal loads that cause significant stress/pressure fluctuations or when dealing with non-dissipative materials (i.e., elastic materials). It is because SPH solves the fully dynamic momentum equation of the continuum field using the fully explicit time integration scheme. This type of numerical solution is well-known to be vulnerable to free-fluctuation caused by inertial forces and also occurs in other numerical methods (e.g., FEM, MPM), which solve the fully dynamic momentum equation. A simple remedied approach is incorporating a viscous damping force into the momentum equation to remove undesirable fluctuations. Among several viscous damping formulas proposed in the literature, the following equation proposed by Bui et al. [52] can be adopted:

$$F_d = -\mu_d \mathbf{v}_{ij} \quad (86)$$

where  $\mu_d = \vartheta \sqrt{E/\rho_s h^2}$  is the damping coefficient, with  $\vartheta$  being the non-dimensional damping coefficient, whose recommended value is  $\vartheta = 0.02$  [52]. In this paper, the above viscous damping force is only adopted in cases involving elastic materials. For problems involving elastoplastic materials, the viscous damping force is only adopted to achieve the initial in-situ stress conditions. Once the desirable stress conditions are achieved, this damping force is removed from the momentum equation to avoid undesirable influence on the dynamic motion of SPH particles (i.e., energy dissipation).

#### 3.4.2. Stress and pore-fluid pressure regularisations

It is commonly known that the traditional SPH method suffers from the so-called short-length-scale noise in the pressure field, which Monaghan first identified in the context of fluid mechanics [100]. In the computational geomechanics context, when SPH is applied to simulate large deformation and failure of geomaterials, a similar issue was reported in the pressure/stress fields of SPH particles undergoing large shear deformation [105], which was discussed in depth in Bui and Nguyen [26]. Although the stress noise does not please the eye, it does not produce pronounced influences on the kinematics of SPH particles [23,52,105], thanks to the SPH approximation procedure, which automatically filters out the stress oscillation. However, to further stabilise the SPH solution and produce a smooth stress profile, the following Shepard stress regularisation technique can be applied [26,105]:

$$\sigma_i^{new} = \frac{\sum_j^N V_j \sigma_j W_{ij}}{\sum_j^N V_j W_{ij}} \quad (87)$$

where  $\sigma_i^{new}$  is the regularised stress of particle  $i$  and is equivalent to the mean stress of all SPH particles located within the supporting domain of particle  $i$  weighted by the kernel function. It has been previously demonstrated that this stress regularisation improves the stability of SPH and produces stable results. However, the main drawback of this stress regularisation approach is that the stress field variable may be over-regularised for long-time simulations involving many computational cycles. Therefore, it is recommended that this stress regularisation should only apply after specific computational cycles, which need to be tested on a case-by-case basis to avoid over-regularisation. For applications reported in this paper, stress regularisation is applied after every 5000 steps.

On the other hand, when solving the fully coupled hydro-mechanical ( $u - p$ ) governing equations of saturated porous media, it is commonly reported in the literature that most numerical solutions exhibit spurious pore-pressure oscillations, and alternative treatments are often required. This issue is not an exception in SPH, and it may even become more severe given that both pore-water pressure and displacement fields are evaluated at the same location. In our proposed SPH scheme, such the pore-pressure oscillation only occurs in some exceptional cases, involving

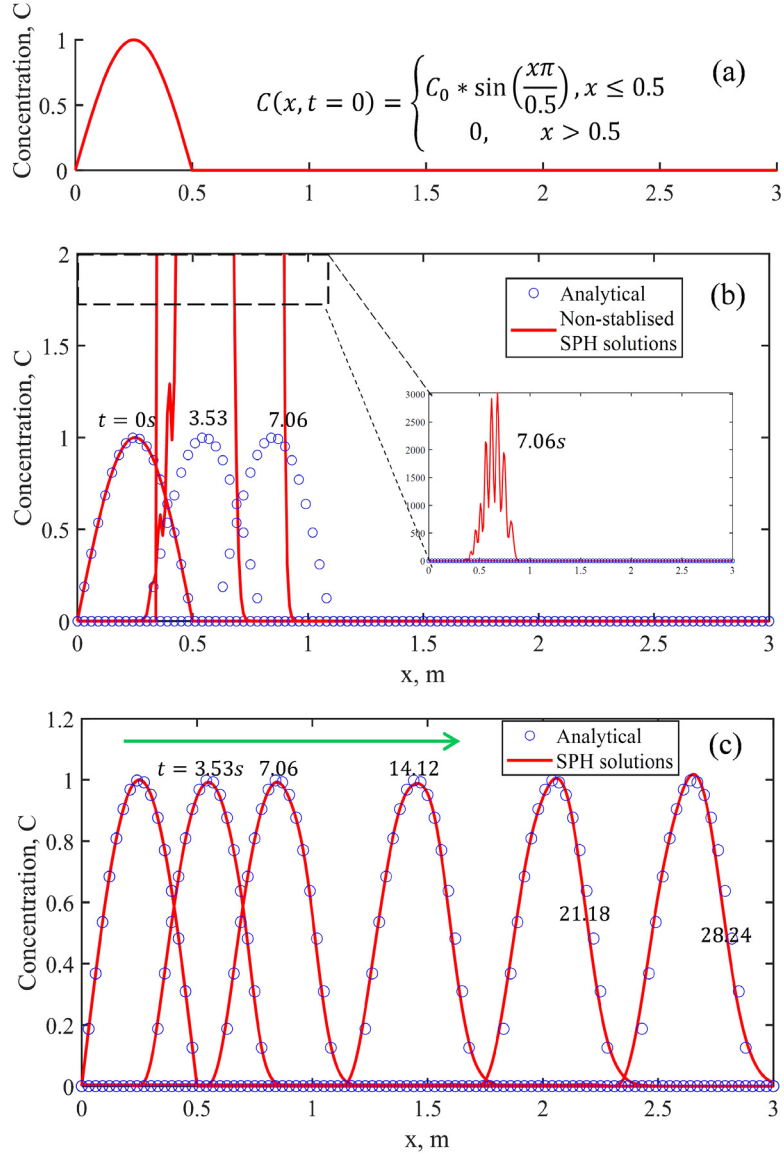


**Fig. 3.** Performance of the proposed SPH scheme for the pure-convection flow problems.

very low permeability or under undrained conditions, thanks to the accurate SPH approximations. To overcome this issue in those exceptional cases, a similar stress regularisation approach can be adapted to the correct pore-water pressure oscillation by applying the following formulation:

$$p_{fi}^{new} = \frac{\sum_j^N V_j p_{fj} W_{ij}}{\sum_j^N V_j W_{ij}} \quad (88)$$

where  $p_{fi}^{new}$  is the regularised pressure. In this paper, since we do not involve any problems with very low permeability, this pressure regularisation is not required, though it can be adopted.

#### 3.4.3. Treatment of numerical instability in convection-dominated flow problems

Finally, when solving the transport equation, i.e., Eq. (25) or Eq. (76), which involves convection-dominated flows, non-physical spatial oscillations of numerical solutions (so-called ‘wiggles’) often occur regardless of the

types of numerical methods [106,107]. Special treatments are often required to address this issue, and several techniques have been proposed for the finite element method [17,108]. The above issue is not an exception in SPH, although the SPH method was previously demonstrated to have advantages in solving the convection–diffusion problems [102], thanks to its Lagrangian nature and inherent non-local feature of SPH formulations. However, in several exceptional cases involving pure-convection flow problems, such as Eq. (25), non-physical spatial oscillations in numerical solutions might still occur in SPH, and particular treatment is thus required. Eq. (25) can be rewritten in the following general form for the pure convection-flow problem:

$$\frac{dC}{dt} + \mathbf{v} \cdot \nabla C = f(\mathbf{v}, C) \quad (89)$$

where  $C$  is the concentration;  $\mathbf{v}$  is the flow velocity; and  $f(\mathbf{v}, C)$  is the source term. Here, to compare our numerical solutions against existing analytical solutions, we will assume  $f(\mathbf{v}, C) = 0$ . As a result, the 1D analytical solution for the above convection equation in this standard case is  $C(x, t) = C_0(x - vt)$ , where  $x$  is the spatial distance,  $t$  is the time, and  $C_0 = C(x, 0)$  is the initial concentration at  $t = 0$ .

The SPH approximation of the above pure convection flow equation can be straightforwardly written as follows:

$$\frac{dC_i}{dt} + \mathbf{v}_i \cdot \sum_{j=1}^N V_j (C_j - C_i) \hat{\nabla}_i W_{ij} = f_i(\mathbf{v}, C) \quad (90)$$

The numerical solution of the above equation can be obtained by integrating this equation following the standard leap-frog algorithm explained in Section 3.3. For the initial condition shown in Fig. 3(a), the comparison between SPH and analytical solutions is shown in Fig. 3(b) for the velocity of  $\mathbf{v} = 0.0085$  m/s and  $f(\mathbf{v}, C) = 0$ . The 1D SPH solutions were achieved by using an initial particle spacing of  $dx = 0.01$  s and the time step of  $dt = 0.0005$  s. It can be seen that the SPH solution highly fluctuates and does not reproduce the analytical solution. To address this issue, a simple approach is to regularise the concentration using the following equation:

$$C_i^{new} = \frac{\sum_j^N V_j C_j W_{ij}}{\sum_j^N V_j W_{ij}} \quad (91)$$

Similar to stress regularisation, the regularisation of concentration should only be applied after a certain number of computational cycles to avoid over-regularise the expected value. A specific number will depend on specific applications and require careful consideration. For example, the SPH solution could reproduce well the analytical solutions by applying the regularisation of concentration after every 160 timesteps, as shown in Fig. 3(c). For applications in this paper, different SWCCs produce different flow characteristics depending on the difference in the hydraulic conductivity between saturated and unsaturated zones. As a result, the fluctuation of concentration is only observed in exceptional cases where the SWCC produces a substantial difference in the hydraulic conductivity between saturated and unsaturated zones, resulting in a very steep seepage velocity difference at the interface between the unsaturated and saturated zones, thus causing oscillations in the predicted concentration. In such cases, the regularisation of concentration will be applied, and the specific regularisation number varies for each case, which will be specified for each application.

## 4. Numerical results and discussions

### 4.1. Performance of the proposed suction/erosion-dependent constitutive model

The performance and accuracy of numerical implementation of the proposed constitutive model are verified by conducting an SPH simulation of a simple shear test, and numerical results are compared with those obtained from the single-element test using Matlab. The geometry and setting conditions of the simple shear test are shown in Fig. 4(a). In this test, a representative soil element is placed in the central area and surrounded by boundary areas. The soil element and boundary are modelled by a set of SPH particles with the same soil properties. Particles within the central area are allowed to move freely, while a constant velocity field (i.e.,  $v_{xi} = \vartheta y_i$  and  $v_{yi} = 0$ ) is enforced to those particles within the boundary area, where  $\vartheta$  is a constant parameter controlling the loading rate. The corresponding loading path imposed on the representative soil element is shown in Fig. 4(b) for different

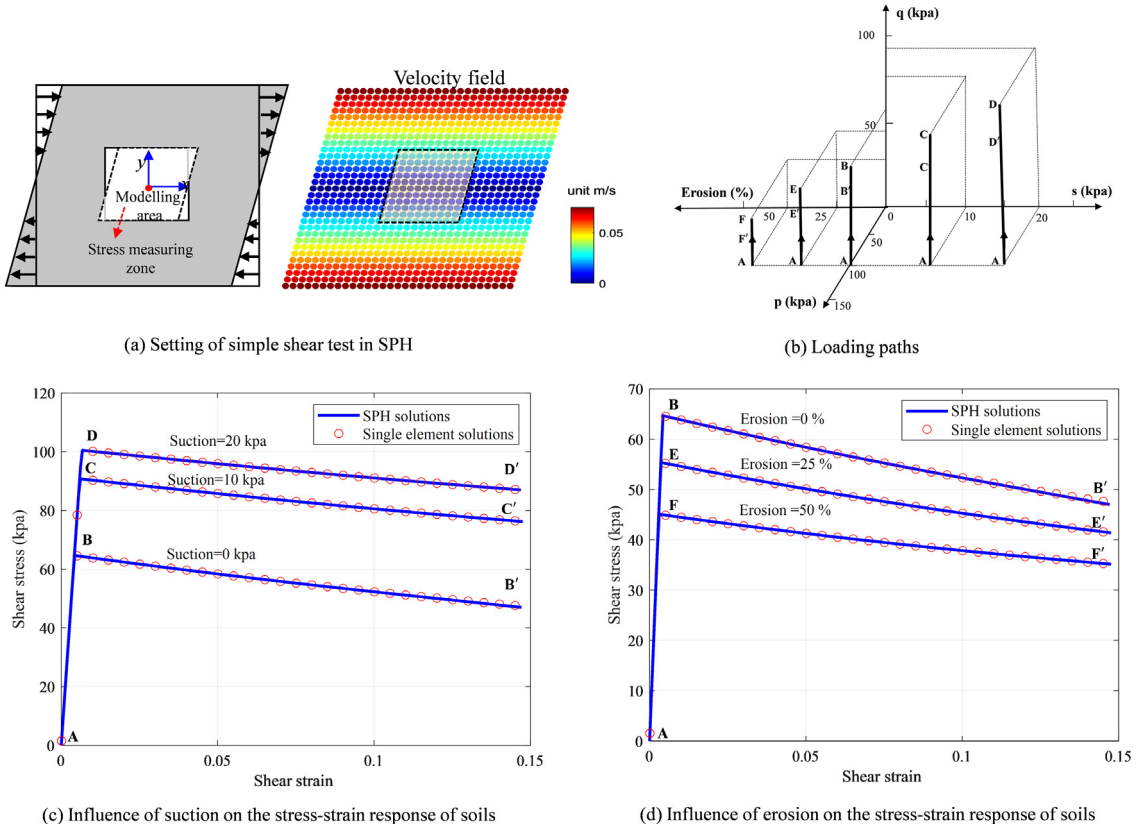


**Fig. 4.** Performance of the proposed constitutive model at the element level and in SPH.

suctions (0, 10 kPa, 20 kPa) and degrees of erosion (0%, 25%, 50%). The degree of erosion corresponds to the amount of fines content eroded from the soil sample. Fig. 4(c) and (d) compare the stress–strain relationship between the SPH and single-element solutions for different suctions and degrees of erosion, respectively. The influence of suction and erosion on the shear strength of the simulated soils was demonstrated in the proposed constitutive model, with a higher suction producing higher shear strength while more erosion causes a reduction in the peak strength of the materials. In both cases, the strain-softening process was well predicted with large shear deformation. The SPH solutions agree well with the single-element results, suggesting that our numerical implementation of the new constitutive model in SPH is correct.

#### 4.2. One-dimensional consolidation test

A one-dimensional (1D) consolidation test of a fully saturated soil sample is simulated in this section to verify the capability of the proposed SPH framework in capturing the fully coupled flow-deformation problem. The soil sample of 1 m high and 0.1 m width is discretised by SPH particles with an initial particle distance of 0.01 m. Soil is assumed to be homogeneous and linear elastic material with the following properties: Young's modulus  $E = 2 \times 10^7$  Pa, Poisson's ratio  $\nu = 0.33$ , soil particle density  $\rho_s = 2000 \text{ kg/m}^3$ , initial porosity  $n = 0.36$ , initial permeability coefficient  $k_w = 1 \times 10^{-4} \text{ m/s}$ , fluid bulk modulus  $K_f = 2 \times 10^9 \text{ Pa}$ , and time step  $\Delta t = 1 \times 10^{-7} \text{ s}$ . The left and right boundaries are set to the free-slip boundary condition, while the bottom boundary is no-slip or fully fixed. The SPH simulation consists of two consecutive stages. Firstly, all boundaries are set to the undrained condition, and a stress of 10 kPa is applied to SPH particles on the top layer. The applied stress is converted into acceleration and linearly increased in a short period of 0.01 s (i.e., ramp-load) to avoid oscillations caused by the sudden load. At the end of the ramp-load stage, the pore-water pressure inside the soil sample reaches 10 kPa, while the effective stress remains almost 0 kPa. In the second stage, the top boundary of the soil sample is changed to the

drained condition, while the applied stress is maintained at 10 kPa. As a result, the pore water pressure inside the soil sample gradually decreases and transfers to the effective stress, causing the soil sample to deform vertically. As discussed in the earlier section, since we are dealing with the non-dissipative linear elastic material, viscous damping ( $\vartheta = 0.02$ ) is adopted to suppress stress and pore-water pressure fluctuations.

Both proposed momentum equations (34) & (36) are tested, and the comparisons between SPH results and analytical solutions for the 1D consolidation test in terms of pore water pressure variation at different time factors and the degree of consolidation are shown in Fig. 5, where the time factor is computed by  $T_v = \frac{km_v}{\rho_w g H^2} t$  with  $m_v$  being the constrained modulus defined by  $m_v = \frac{E(1-v)}{(1+v)(1-2v)}$ ,  $k$  being permeability coefficient (m/s), and  $H$  being the soil column height (m). It can be seen that the proposed SPH model matched very well with the analytical solutions for both the pore-water pressure dissipation process and the degree of consolidation, which is calculated for surface particle settlement. Both momentum equations (34) & (36) used in SPH lead to similar numerical results. The minor difference between SPH and the analytical solutions at the early stage of pore-water pressure dissipation can be attributed to the natural difference between the fully dynamic SPH simulation and quasi-static assumption in the analytical solutions. Nevertheless, there exist minor differences between two SPH solutions using different momentum equations at  $T_v = 0.005$  and  $T_v = 0.01$  (Fig. 5a) for a relatively large permeability coefficient of  $k = 10^{-4}$  m/s. This might be attributed to the consideration of drag force when using the solid phase momentum equation. These minor differences vanish when the permeability coefficient becomes lower, for example, in the case of  $k = 10^{-6}$  m/s when the influence of drag force is negligible (Fig. 5c). A similar observation was also reported in the study of Morikawa and Asai [28] when they solved a similar momentum equation of the solid phase using u-w-p (soil's displacement, Darcy's velocity, pore water pressure) formulation.

#### 4.3. One-dimensional transient seepage flow

This test aims to demonstrate the predictive capability of the proposed SPH numerical framework in capturing the transient seepage flows in unsaturated soils. Here, the one-dimensional infiltration test previously simulated by Gardner [109] using FEM is reproduced by SPH. In this simulation, a soil column of 3 m in height was created using SPH particles with an initial distance of 0.02 m. A linear negative pore water pressure  $p_w = -\rho_w g z$  was applied to the soil column to represent the initial suction condition. Subsequently, a constant flux of  $Q = 0.1$  m/day was applied at the top surface. The following soil properties were adopted in the simulation: permeability coefficient is  $k_{sat} = 1.0$  m/day, water bulk modulus is  $K_f = 2 \times 10^9$  Pa, the porosity is 0.4, and the time step is  $dt = 1 \times 10^{-5}$  day. The following SWCC and permeability coefficient functions previously used by Gardner [109] were adopted for the comparison purpose:

$$\begin{aligned} S_r &= S_{res} + (S_{sat} - S_{res}) \cdot \exp(-g_a|h|) \\ k &= k_{sat} \cdot \exp(-g_a|h|) \end{aligned} \quad (92)$$

where  $S_{sat} = 1$ ,  $S_{res} = 0.23$ ,  $g_a = 2 \text{ m}^{-1}$ , and  $k_{sat} = 1 \text{ m/day}$ .

Fig. 6(a) shows the time evolution of the total water pressure head in the soil column. The applied water flux on the top surface forces the water to migrate downward, gradually increasing the total water pressure head in the soil column from top to bottom. Fig. 6(b) shows the time evolution of the suction head (i.e., negative pore water pressure head) at different elevations. The soil on the top surface gradually became saturated as suction reduced, and the saturation progressively propagated to the bottom of the soil column. The SPH solution matched very well with the FEM counterpart, demonstrating that our framework can accurately predict the transient unsaturated seepage flow. Next, our proposed computational framework will be evaluated for its capability to predict internal erosion caused by transient seepage flows in both steady and unsteady flows.

#### 4.4. Prediction of Sterpi's erosion test

This section demonstrates the predictive capability of the proposed numerical framework in predicting the erosion process by simulating Sterpi's erosion tests, which were previously conducted on fully saturated soil specimens subjected to different hydraulic heads [74]. In the experiment, the soil sample was reconstituted in a cylinder mould of 7 cm in diameter and 14 cm in height, as shown in Fig. 7(a). It was connected with the upper and lower reservoirs by inlet and outlet tubes so that the hydraulic gradient could be applied and kept constant during the test. A sieve

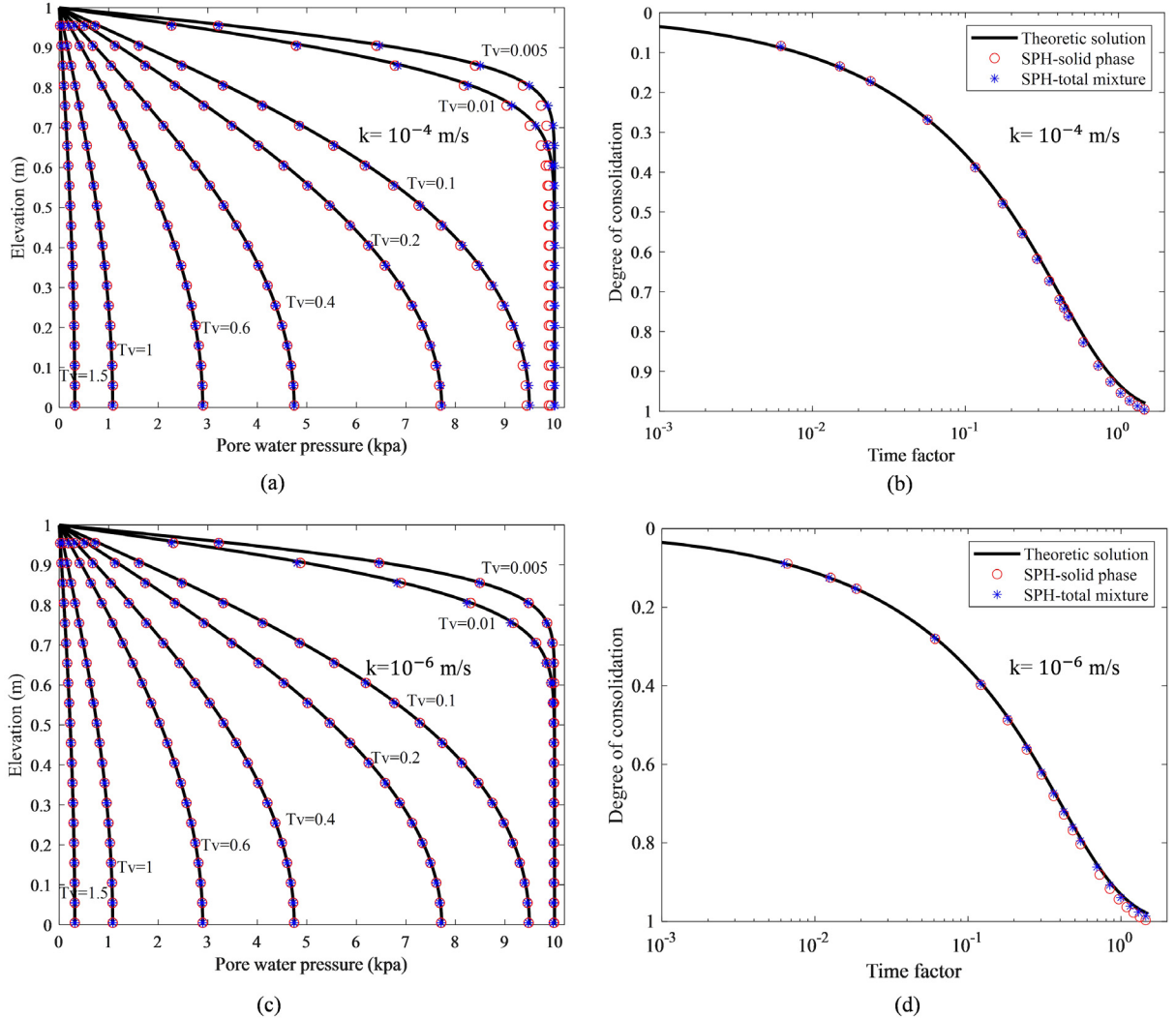
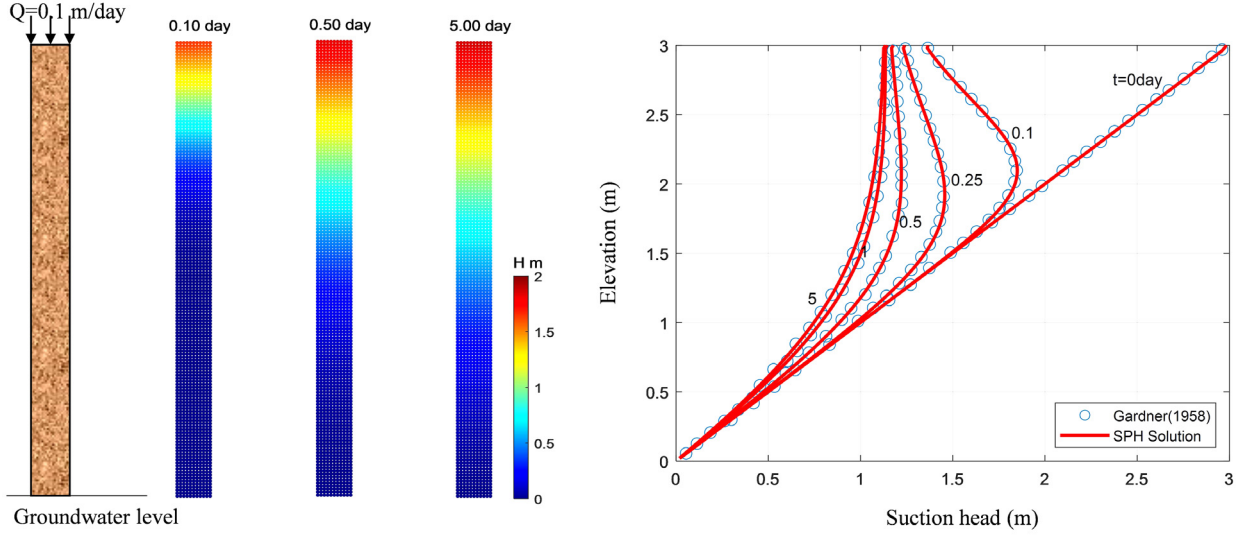


**Fig. 5.** Comparison between SPH results and analytical solutions for one-dimensional consolidation test: (a) and (c) variation of excess pore water pressure; (b) and (d) degree of consolidation.

was placed above the lower reservoir to collect the eroded fine particles. The weight of the eroded fine particles was measured after oven drying. In this test, the upward seepage flow was applied to prevent the potential of clogging due to transported fine particles by a downward flow. Five testing cases were carried out with various hydraulic gradients, two of which were conducted for up to 50 h. The saturated permeability coefficient of non-eroded soil is 0.36 m/h, which is assumed constant. The initial fines content is 0.2, and the porosity is 0.34.

As noticed from the above experimental setting conditions, Sterpi's test is only suitable to investigate the influence of the hydraulic gradient on the internal erosion process. Moreover, because of these experimental setting conditions (i.e., small soil specimen and no confining stress), the influence of mechanical deformation on the hydraulic properties and eroded fines are negligible. For this reason, our SPH simulations assumed the soil as a rigid body; thus, no coupled hydro-mechanical analysis is required in this test. In the SPH simulations, the soil sample was discretised using 2,450 SPH particles with an initial particle distance of 0.2 cm. The simulation starts from a steady-state seepage flow condition with a constant hydraulic gradient imposed across the soil specimen and a zero pore-fluid pressure imposed on the top surface to represent the overflow condition. Under these setting conditions, the internal erosion process was immediately triggered after the simulation started. The erosion will stop when the



(a) Evolution of total water pressure head

(b) Comparisons between SPH and FEM solutions

**Fig. 6.** Comparisons between SPH and FEM for the solutions of transient unsaturated seepage flows.

fines content is smaller than its residual value to mimic the experimental condition. The time step of  $1 \times 10^{-3}$  h was adopted in all simulations.

**Fig. 7(b)** compares the SPH simulations and experiments for several erosion tests with different hydraulic gradients. In the simulations, Erosion law (1) listed in [Table 1](#) was adopted, but its ultimate fines content ( $f_{\infty}$ ) follows that proposed by Sterpi [74]. The hydraulic and erosive parameters required for this erosion law were calibrated from the erosion test using a hydraulic gradient of 0.55, giving  $\lambda_e = 0.25$ ,  $f_{c0} = 0.2$ ,  $a = 4.02$ ,  $b = 0.5$ ,  $c = 2.64$ . These calibrated parameters were subsequently adopted in all other SPH simulations for different hydraulic gradients. The percentage of erodible fines reported in the figure was computed based on the mass loss caused by internal erosion.

In the experiment, the fines start eroding when the hydraulic gradient equals 0.18, which can be regarded as the critical hydraulic gradient triggering internal erosion for the tested soil. Under a constant hydraulic gradient, the eroded fines content increases and gradually reaches a maximum erodible fines content after around 30 h. The maximum erodible fines content represents the limit of erosive ability, dependent on the soil strength and its hydraulic gradient. A larger hydraulic gradient can cause an increase in the erosive ability, with more fines can be eroded if time is enough. The SPH simulations could quantitatively capture the above observations reported in the experiments and the mass loss due to seepage erosion compared to the experiment. However, the simulations underestimate the prediction of eroded fines for tests with high hydraulic gradients (i.e.,  $i = 0.75$ ). This difference can be attributed to the suitability of erosion law adopted in the numerical simulations and the discussion of which is beyond the scope of this work.

#### 4.5. One-dimensional transient seepage erosion

The capability of the proposed SPH framework in capturing the internal erosion caused by the transient seepage process is illustrated in this section by simulating the 1D infiltration erosion and deposition test. In this test, a simulation of the water infiltration process is conducted on a 6 m soil column. The soil properties are: initial fines mass fraction 0.2, porosity  $n = 0.36$ , concentration  $C = 0$ , and fluid bulk modulus  $K_f = 2 \times 10^9$  Pa. The initial pore fluid pressure inside of the soil column distributes linearly ( $p_f = -\rho_f g z$ ). During the test, the pore fluid pressure at the bottom surface is maintained at 0 Pa (permeable boundary), and a constant pore water pressure head of  $h = 4$  m is applied to the top surface. The concentration of fluidised particles on the top surface was kept at zero during the test to replicate an assumption of clear water infiltrated into the soil column. In the SPH simulation, the

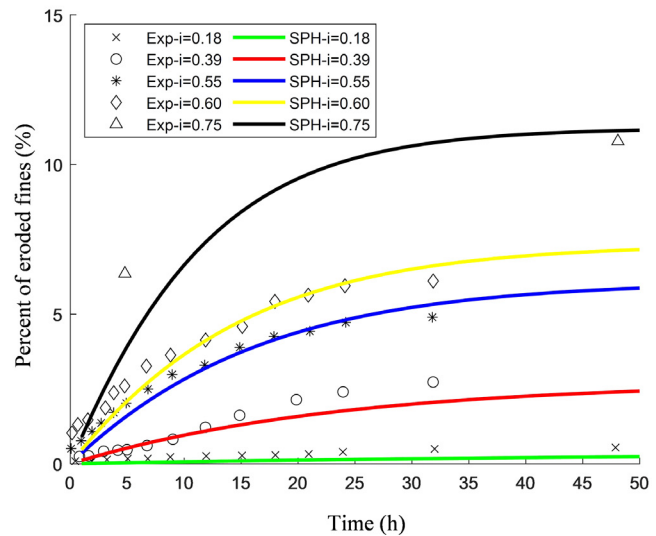
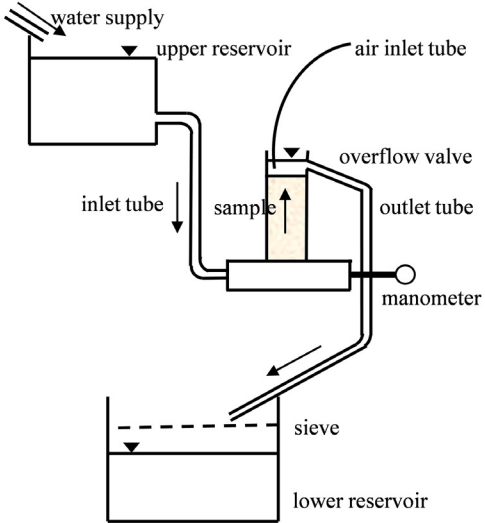


**Fig. 7.** Sterpi's erosion test.

**Table 4**

Hydraulic parameters used in SPH simulation.

$K_{sat0}$ (m/h)	$\phi_0$	$n_r$	$k_a$	$k_r$	$m_{e0}$ ( $\text{kg}/\text{m}^3$ )	$S_{min}$
0.18	0.36	3	0	0.012	340	0
$k_e$	$f_{c0}$	$k_d$	$g_a$ ( $\text{m}^{-1}$ )	$g_n$	$K_f$ (Pa)	$S_{max}$
0.4	0.2	0.2	0.5	1.8	$2 \times 10^9$	1

soil column is discretised using SPH particles with an initial particle spacing of 0.08 m, which requires the time step of  $1 \times 10^{-8}$  h. The relationship between permeability coefficient and suction force follows the same form as that proposed by Gardner [109]:

$$k = \exp(-g_a|h|)k_{sat} \quad (93)$$

where  $g_a$  is a constant parameter;  $h$  is the suction head; and  $k_{sat}$  is the permeability coefficient at the fully saturated condition. In this erosion and deposition test, the value of  $k_{sat}$  changes with different degrees of erosion and deposition, and to account for this phenomenon, the saturated permeability coefficient  $k_{sat}$  is updated by the modified Kozeny–Carman relationship [18,110]:

$$k_{sat}(\phi, C) = k_{sat0} \frac{[(1 - f_r)k_a + f_r\phi/\phi_0]^{n_r}}{1 + 2.5C} \quad (94)$$

$$f_r = 1 - k_r m_{de}$$

where  $k_{sat0}$  is the initial permeability coefficient;  $k_a$  is a parameter accounting for the residual permeability;  $n_r$  is an index ranges between 2.5 and 3.5;  $f_r$  is a flow efficiency factor;  $\phi$  is the current porosity;  $\phi_0$  is the initial porosity;  $k_r$  is the coefficient of flow efficiency for fine particles;  $m_{de}$  is the deposited fines mass, which can be directly computed from the deposition rate;  $C$  is the concentration. In summary, the hydraulic parameters used in this SPH simulation are listed in **Table 4**.

In the first test, the mechanism of the pure internal erosion process (i.e., without deposition) is simulated by SPH using Erosion law (1) listed in **Table 1**. In this case, the ultimate fines content was set to zero as a relatively large hydraulic gradient was considered. On the other hand, as water infiltrates the soil column, fines could be eroded, turning into fluidised particles and transported through pores. The migration of fluidised particles within the soil column causes deposition, which influences the internal erosion rate and causes further changes in the hydraulic

properties of soils. For this reason, the second test additionally considers the influence of fines deposition on the erosion mechanisms by incorporating deposition law (1) in the simulation. The results of both testing cases are plotted in Fig. 8, together with the reference results of the pure seepage infiltration process without internal erosion where applicable.

In the pure internal erosion case, as the water infiltrates through the soil column and the critical hydraulic condition is reached, the internal erosion process is progressively triggered from top to bottom, resulting in the variations of fines content and porosity distribution along the soil column, as shown by the red solid-lines in Fig. 8(a) and Fig. 8(b), respectively. The soil close to the top surface experiences the most internal erosion, reflecting the commonly known surface coarsening phenomenon [111]. As the fines are further eroded from the top surface, turned into fluidised particles and transported with the seepage flow towards the bottom of the soil column, the concentration of fluidised particles progressively develops, as shown in Fig. 8(c). Unlike the evolution of fines content, the concentration gradually increases from zero on the top surface to a peak value and then reduces. The evolution of concentration closely follows the development of saturation inside the soil column, as shown in Fig. 8(d), which is directly linked to Darcy's velocity, controlling the rate of erosion and concentration. The fully saturated zone enlarges from the upper soil column as the seepage flow further progresses downward, leading to an increase in the seepage velocity, which facilitates the development of internal erosion in the upper soil column. As a result, more fluidised particles are generated and transported downwardly, causing a further increase in the peak value of concentration, as shown in Fig. 8(c). The position of peak concentration is also progressively shifting downward as the saturation zone enlarges but has a time delay.

The influence of internal erosion on the transient seepage flow and hydraulic properties is visible in Fig. 8(d)–(f) compared to the pure infiltration case without internal erosion (i.e., black dash lines). Erosion causes changes to the porosity and concentration, which are directly linked to the rate of change of seepage infiltration through the water permeability described by Eq. (94). As a result, the permeability within the fully saturated zone significantly increases with internal erosion, as shown in Fig. 8(e). The permeability increase facilitates the development of the seepage front and the pore-water pressure compared to the pure infiltration case, as shown in Fig. 8(f), respectively. Internal erosion modifies the pore-water pressure distribution in the fully saturated zone (i.e., after 1 h infiltration), changing from a linear distribution for the case without internal erosion to a non-linear distribution under continuous erosion, reflecting the continuous change of hydraulic conductivities and thus Darcy's velocity as well as fluid density within the saturated zone. It is noted that although the evolution of concentration was solved in this case, it does not contribute to the erosion mechanism controlled by erosion law. In other words, the concentration was developed in the fluidised-particle phase, but it was not deposited back into the solid phases. As a result, no clogging phenomenon commonly caused by internal erosion was observed in this case. Therefore, the contribution of deposition to the solid phase needs to be considered to adequately describe the consequences of the internal erosion process on the hydraulic properties of soils.

The influence of deposition is now considered by accounting for the contribution of deposition to the erosion law. Fig. 8 compares the results of this case, shown by blue dash lines, and those previously reported for the cases with pure erosion. Unlike the pure erosion case, the deposition now contributes to the erosion law and the hydraulic permeability described by Eq. (94), thus completely altering the internal erosion mechanisms. At the early stage of internal erosion (i.e.,  $t < 0.2$  h), the contribution of deposition has a minimal impact on the evolutions of fines content and porosity, as shown in Fig. 8(a)–(b). However, as the seepage flow further progressed downward, more fluidised particles (concentration) were developed, transported with the seepage flow, and turned into deposition. The deposition process turns fluidised particles into erodible-fines particles, compensating for the mass loss, thus reducing the overall loss of fines content in the system compared to the pure erosion case, as shown in Fig. 8(a). The increase in porosity caused by internal erosion also reduces because of the contribution of deposition generated in the flow, as shown in Fig. 8(b). After  $t = 0.4$  h of seepage infiltration and erosion/deposition, the distribution of fines content and porosity along the soil column becomes heterogeneous (i.e., the distribution curves are no longer smooth), indicating a clogging phenomenon in the system caused by the deposition. This clogging phenomenon was well supported by the evolution of concentration (and thus deposition), degree of saturation and permeability in the system, as shown in Fig. 8(c) to Fig. 8(e), respectively. Compared to the pure erosion case, the inclusion of deposition further delays the seepage flow, leading to the overall reduction of concentration in the system, which can be attributed to the mechanism of mass gain caused by the transportation of fluidised particles with the seepage flow, part of which are deposited back into the solid system (or erodible-solid phase). The concentration develops in

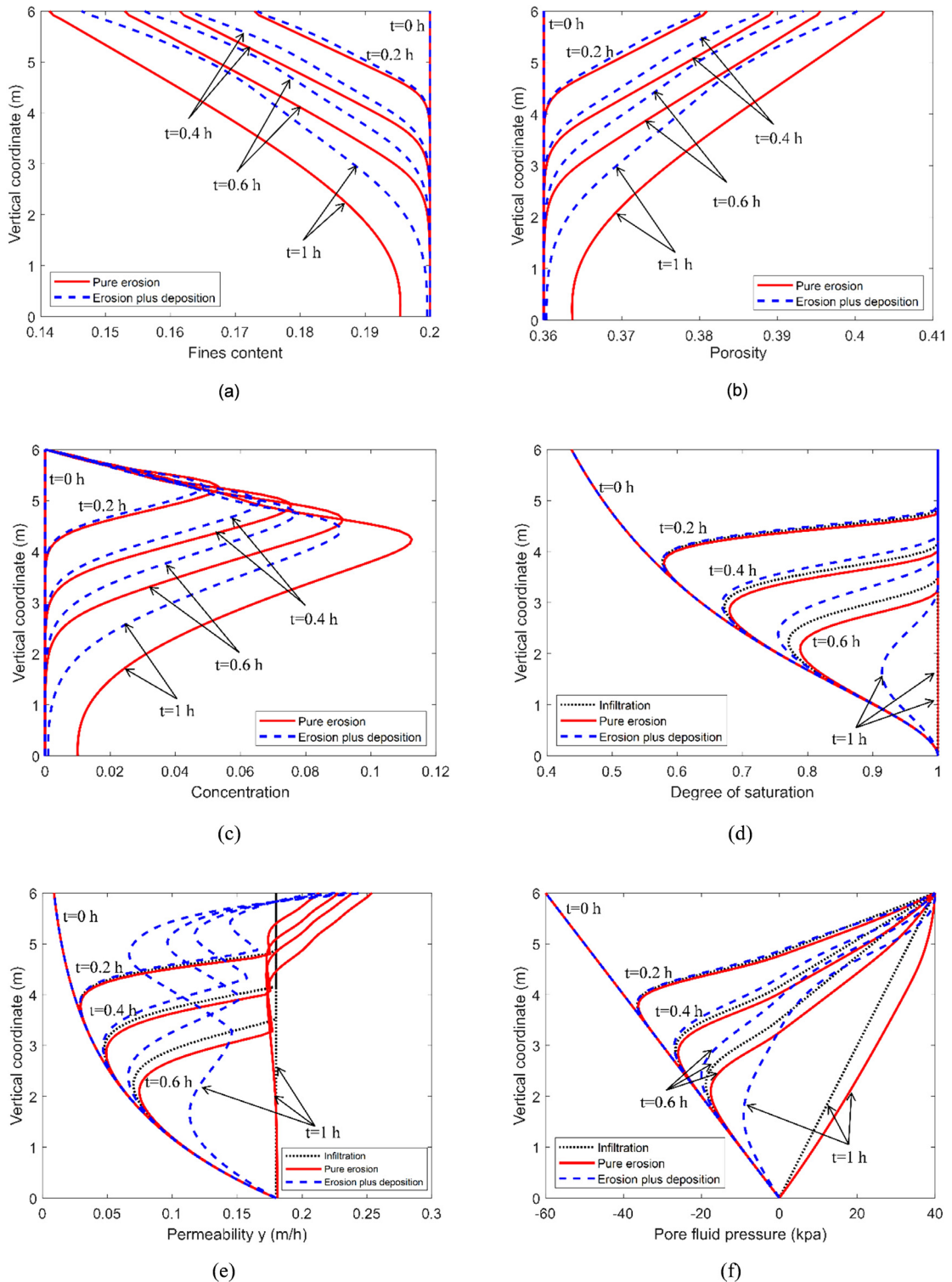


**Fig. 8.** Erosion infiltration process predicted by the proposed SPH-erosion framework: (a) fines content; (b) porosity; (c) concentration; (d) degree of saturation; (e) permeability; (f) pore fluid pressure.

a similar way to that of the pure-erosion case, though its peak value was substantially reduced, which can be again attributed to the mass gain due to deposition. Because a part of fluidised particles (i.e. concentration) is deposited back to the solid phase, the evolution of deposition closely follows that of the concentration but is slightly delayed, as shown in Fig. 9(a) and Fig. 9(c). For example, after  $t = 0.6$  h of seepage infiltration and erosion/deposition, the concentration reaches its peak value at roughly 4.6 m depth, while that of the deposition is around 5.1 m depth, reflecting that not all fluidised particles (or concentration) are deposited back to the solid system. The development of deposition causes a substantial change to the hydraulic permeability of the soil and the net erosion rate, as shown in Fig. 8(e) and Fig. 9(b & d), respectively. Compared to the pure erosion case, the distribution of permeability is highly heterogeneous. Within the fully saturated zone, the permeability reaches its minimum value at the location where the deposition peaks, and subsequently increases following the reduction of deposition. The deposition also caused changes to the permeability in the transition zone between the fully saturated and unsaturated zone, and this can be attributed to the transportation of fluidised particles following the seepage front into the transition zone. The net erosion rate became highly heterogeneous within the fully saturated zone and quickly dropped in the unsaturated zone, as shown in Fig. 9(d), reflecting the clogging phenomenon caused by internal erosion. Finally, the inclusion of deposition completely alters the distribution of pore-water pressure in the system, as shown in Fig. 8(f), reflecting the combined multiple effects due to continuous changes of hydraulic conductivity, net erosion rate, concentration and deposition within the porous system. To this end, it is concluded that the inclusion of deposition rate in modelling internal erosion plays a crucial role in capturing essential mechanisms caused by internal erosion, particularly the clogging phenomenon and heterogeneous distribution of soil properties commonly reported in the internal erosion experiments.

Finally, the influence of different erosion laws on the variations of fine content and concentration is examined with our new model. In this test, Erosion laws (1)–(3) with the same ultimate fines content function are adopted in the simulations. All other material parameters of erosion laws were kept the same for comparison purposes. Fig. 10 shows a comparison of predicted results for different erosion laws. Erosion law (1) produces the highest variation of fines or mass loss and thus causing significant changes to the porosity compared to Erosion laws (2). Erosion law (3) can produce equivalent mass loss compared to erosion law (1) because the ultimate fine's contents are assumed to be zero under a large hydraulic gradient. These results suggest that a suitable erosion law with calibrated parameters is essential in describing the erosion process, which will be explored in future studies.

#### 4.6. Prediction of seepage-induced erosion and failure experiment

In this final test case, a seepage-induced erosion and embankment failure experiment is simulated to demonstrate the capability of the proposed framework in capturing the large-deformation and post-failure behaviour of soils induced by seepage erosion. The experiment was reported in Fox et al. [10,112] and was often referred to as the lysimeter experiment. Fig. 11 shows this experiment's geometry setting and boundary conditions, consisting of a laboratory-scale embankment made of sieved sand constructed in front of a water tank. During the experiment, a constant water head of 30 cm high was imposed on the right boundary of the embankment to simulate inflow water condition, and this was achieved by maintaining the same water level in the water tank. It was reported from the experimental observation that the seepage flow caused internal erosion to occur at the downstream embankment toe and eventually triggered the embankment to collapse. The total time from the initial seepage erosion to the final bank collapse was recorded at 726 s.

To simulate the above experiment, an SPH simulation was conducted under the plane strain condition using the proposed continuum framework for internal erosion and the suction/erosion-strength dependent constitutive model. The embankment was discretised using SPH particles with an initial particle distance of 1 cm. The sand properties and hydraulic constitutive parameters adopted in the SPH model were obtained from the previous experiment, some of which were assumed for a similar soil type ( $d = 0.50$  mm) and listed in Table 5. The viscous damping force ( $\vartheta = 0.02$ ) was adopted to obtain the initial in-situ stress conditions in the embankment but was subsequently removed from the simulation to avoid high energy loss in dissipative materials, as suggested in Section 3.4. To speed up the computational time, a soil elastic modulus of 2 MPa and an equivalent water bulk modulus of  $K_w = 10^5$  Pa were adopted in the simulation to enable a time step of  $1 \times 10^{-4}$  s. In practice, reducing water bulk modulus does not significantly influence the transient seepage flow and large-deformation failure process, which will be examined in Section (4.7). Both erosion and deposition laws (1) were adopted with zero ultimate fines content, and

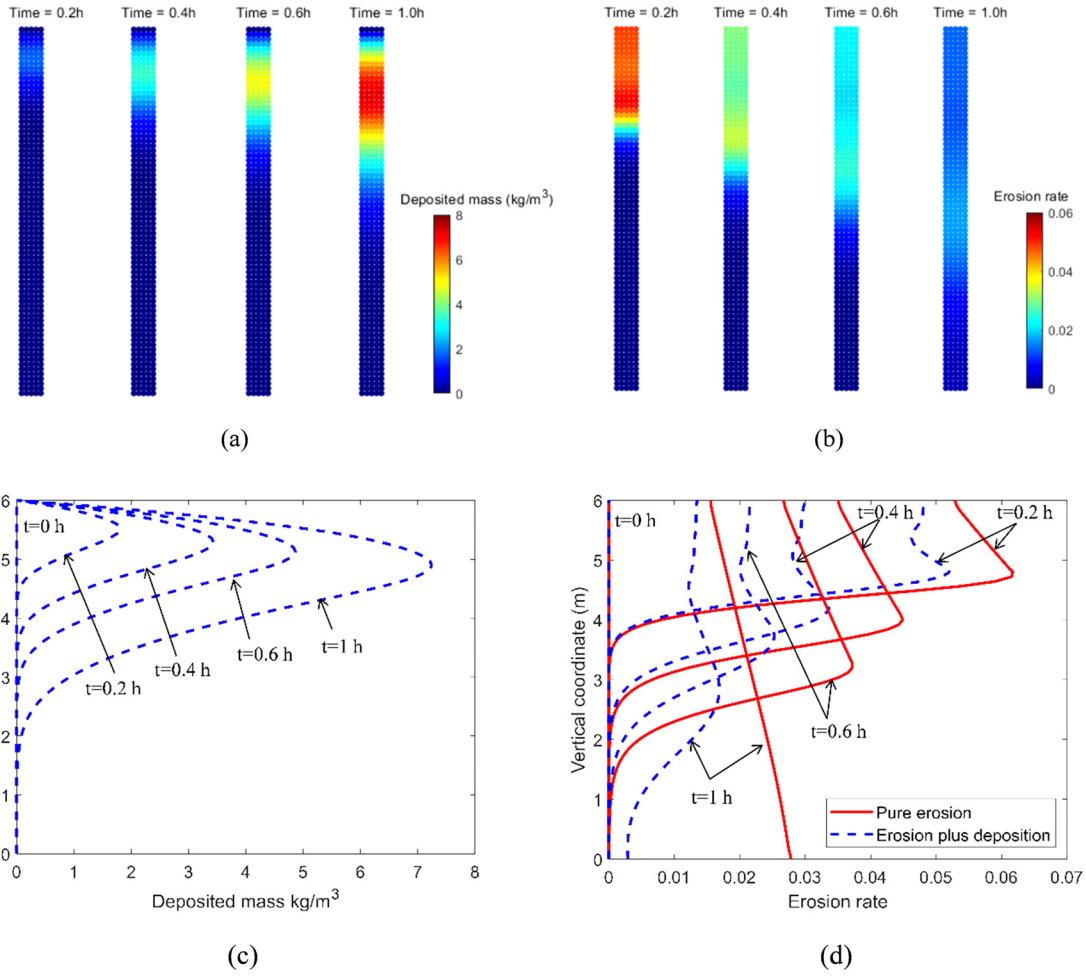


**Fig. 9.** Evolution of deposition and its influence on the seepage velocity.

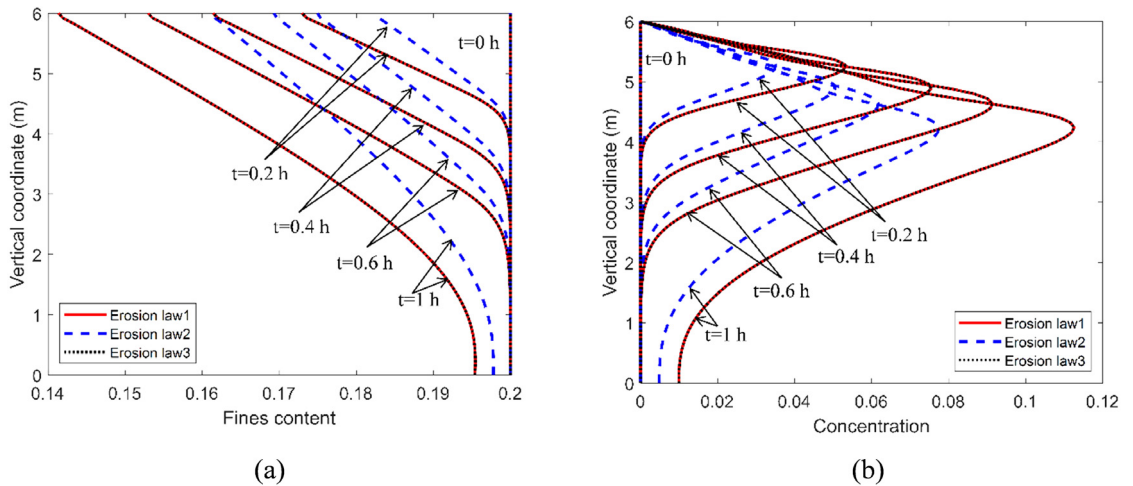


**Fig. 10.** Influence of different erosion laws on the erosion infiltration process.

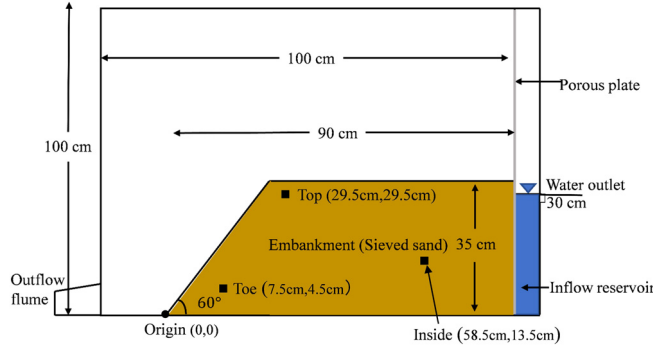


**Fig. 11.** Seepage-induced erosion and failure experiment previously reported by Fox. et al. [10].

**Table 5**

Sand properties and hydraulic model parameters.

Soil type	Sieved sand		
Density $\rho_s$	1900 kg/m <sup>3</sup>	Permeability $k_f$	$3 \times 10^{-3}$ m/s
Young's modulus $E$	2 MPa	Poisson's ratio $\nu$	0.3
Initial fines content $f_{c0}$	0.1	Initial suction force $p_s$	6000 Pa
Saturated saturation $S_{sat}$	1	Residual saturation $S_{res}$	0.075
$g_n$	5	$g_a$	13
$g_l$	-2	Total cohesion $c$	1500 Pa
Effective cohesion $c'$	1000 Pa	Suction dependent cohesion $c_s$	500 Pa
Total friction angle $\varphi$	35°	Suction-dependent friction angle $\phi_s$	0°
Effective friction angle $\varphi'$	35°	Initial Dilatancy angle $\Psi_0$	5°
Residual cohesion	0	Residual friction angle	25°
Porosity $\phi$	0.4	Softening constant $\eta$	2
$B_s$	200	Erosion rate parameter $\lambda_e$	1.2
$\alpha$	25	Deposition rate parameter $\lambda_d$	0.1

Eq. (49) was adopted to update the permeability coefficient for simplicity. The critical hydraulic gradient necessary for triggering internal erosion was commonly in a range of 0.2–0.35 [4,6] for unstable soils and up to 0.5–0.7 for stable soils [4]. The influence of critical hydraulic gradient on the predicted results will also be discussed in Section (4.7). In this section, a critical hydraulic gradient equal to 0.35 was adopted. Dilatancy angle evolves with the material state and vanishes at the critical state, and thus it is assumed to be a function of the equivalent plastic strain  $\psi = \psi_0 e^{-\alpha \varepsilon_p^{eq}}$  [84], in which  $\alpha$  is a constant parameter and is set as 25 and  $\psi_0 = 5^\circ$  is the initial dilatancy angle. In this work, given the insufficient experimental data, this parameter  $\alpha$  is simply selected in numerical simulations to best fit the experimental results.

Fig. 12 shows a qualitative comparison between the experiment and SPH prediction for the evolution of the wetting front inside the embankment. Because a constant water level is imposed on the right boundary, water infiltrates into the embankment, and thus the wetting front develops towards the left-hand side of the embankment. The SPH model could reasonably predict the progression of the wetting front from the early stage of the transient seepage flow till reaching the final steady-state condition. Fig. 13 shows a comparison between the experiment and SPH simulation for the progressive failure of the embankment caused by seepage erosion. In the experiment, seepage erosion first occurs at the embankment toe and loosens the soil strength in this zone. Subsequently, the seepage flow pushes soil particles away from the embankment toe, causing local failure in this zone. The local failure zone enlarges as more soil particles are washed away from the embankment toe, forming an overhang zone on the upper part of the embankment surface. As the seepage erosion progresses further, the retreat of the erodible zone enlarges, causing the entire embankment to collapse. The proposed SPH model could reasonably replicate the above failure mechanisms observed in the experiment, including the formation of seepage erosion zone at the toe caused by the seepage flow, the formation of local failure zone at the toe, the retreat of the erodible zone as the seepage erosion progresses, an overhanging zone and the subsequent embankment collapse. However, the SPH model could

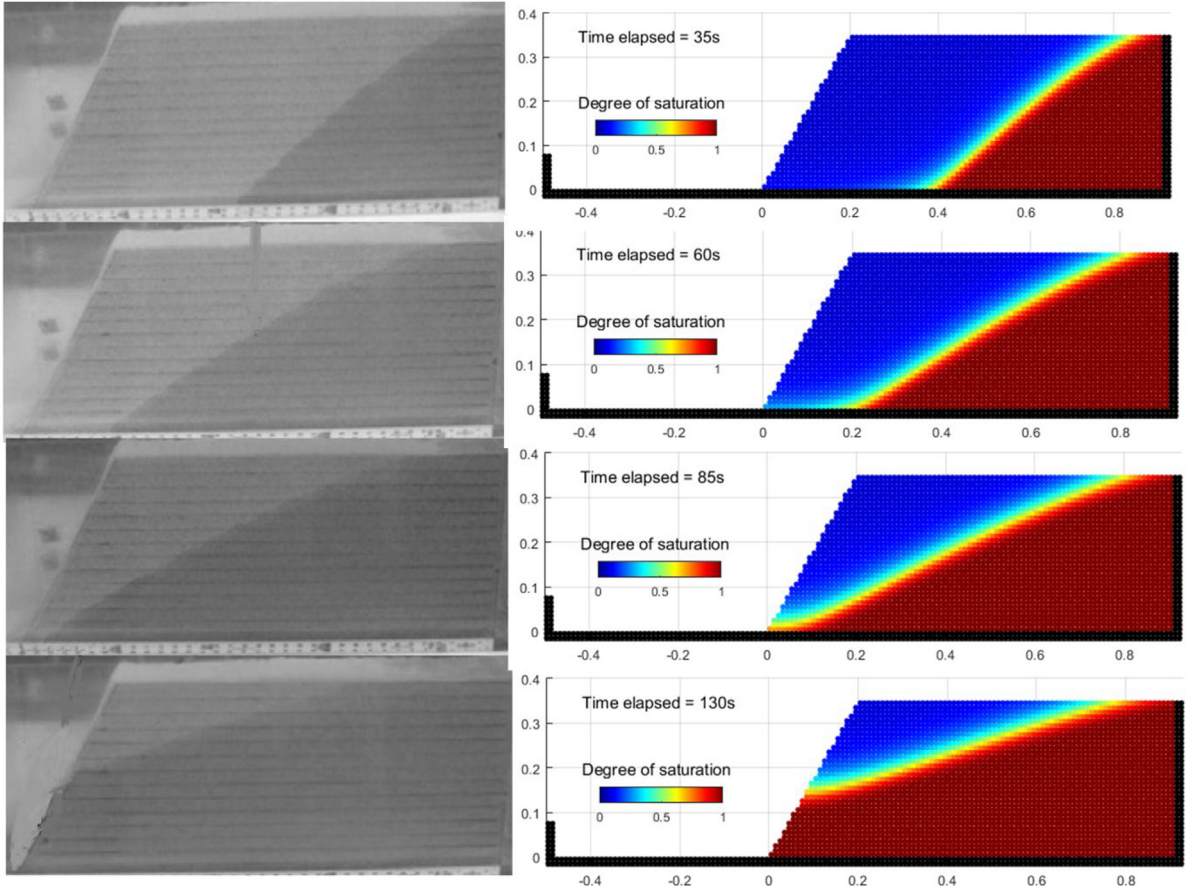


**Fig. 12.** Comparisons of the wetting front between the experiment (after Fox et al. [10]) and SPH modelling.

not capture the tension crack zone observed in the experiment. These discrepancies can be attributed to the missing information on mechanical and hydraulic properties of the simulated soil (e.g., erosion rate, suction force and so on), some of which were not reported in the experiment and thus had to be taken from the literature for the similar soil type. It is noted that, depending on the type of soil and the heterogeneity of the model experiment, the tension crack zone may or may not be observed in the experiment. For example, a similar seepage erosion-induced embankment failure experiment was previously reported by Bui and Nguyen [11], in which an embankment was brought to collapse by seepage erosion at the downstream embankment toe. Though sharing the same mechanism triggering the embankment failure (i.e. seepage erosion at the embankment toe), no tension cracking and overhanging zones were observed in Bui and Nguyen [11]. In fact, the failure mechanisms predicted by the current SPH model are closer to those observed in Bui and Nguyen [11], though they did not report the evolution of the wetting front during the experiment. The evolutions of pore water pressure and effective stress are shown in Figs. 14 and 15, respectively. The pore-water pressure remains stable for the entire seepage erosion process without adopting the pore-fluid pressure regularisation technique. On the other hand, the effective stress exhibits the short-length-scale noise issue when the soil undergoes large shear deformation. Thus, the proposed stress-regularisation technique was adopted after every 5000 computational steps. The smooth and stable distribution of effective stress distribution was subsequently acquired, thanks to the stress regularisation. These results suggest that our proposed stabilisation technique is robust and efficient.

The evolution of fines content and concentration in the embankment caused by the seepage erosion process is plotted in Figs. 16 and 17, respectively, to understand further the influence of erosion on the embankment's failure. During the initial transient seepage flow (i.e., at 100 s), only minor mass loss was observed in the

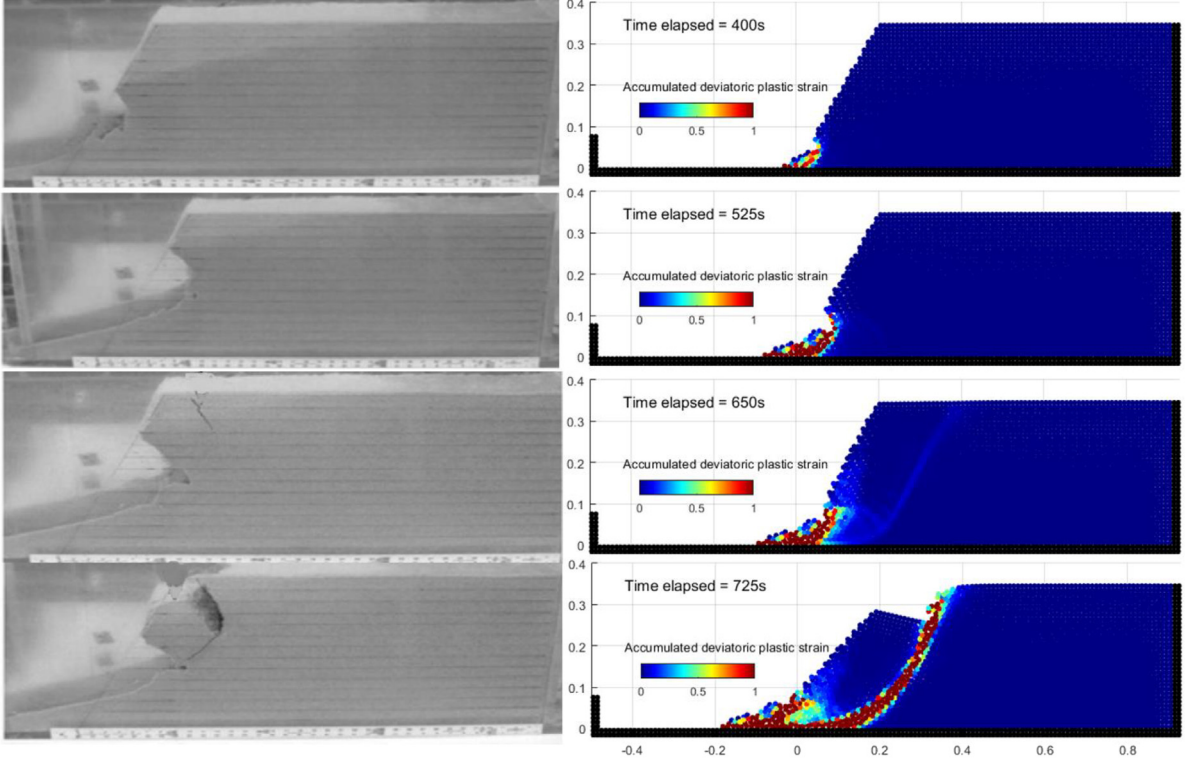


**Fig. 13.** Comparisons (accumulated deviatoric plastic strain) of failure pattern between the experiment (after Fox et al. [10]) and SPH modelling.

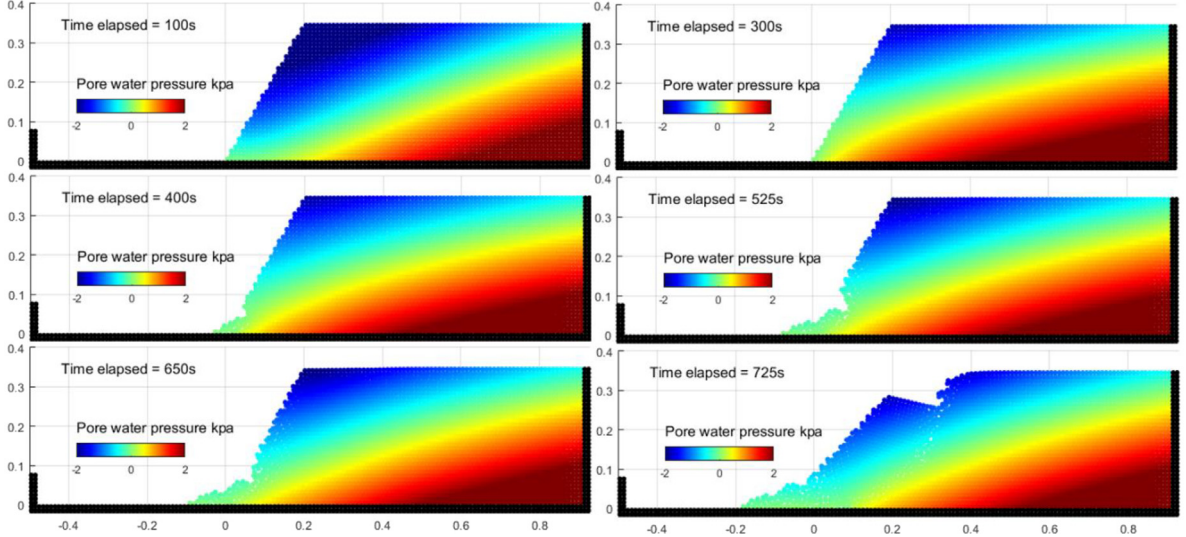


**Fig. 14.** Pore water pressure change during the erosion process.

embankment within the fully saturated zone and the vicinity of the wetting front due to a relatively small seepage velocity. During this period, fluidised particles (or concentration) are gradually transported with the seepage flow towards the slope toe, as shown in Fig. 17. When the seepage flow reaches the embankment toe, the seepage velocity in this zone accelerates and exceeds the critical seepage velocity. This starts triggering the erosion at the

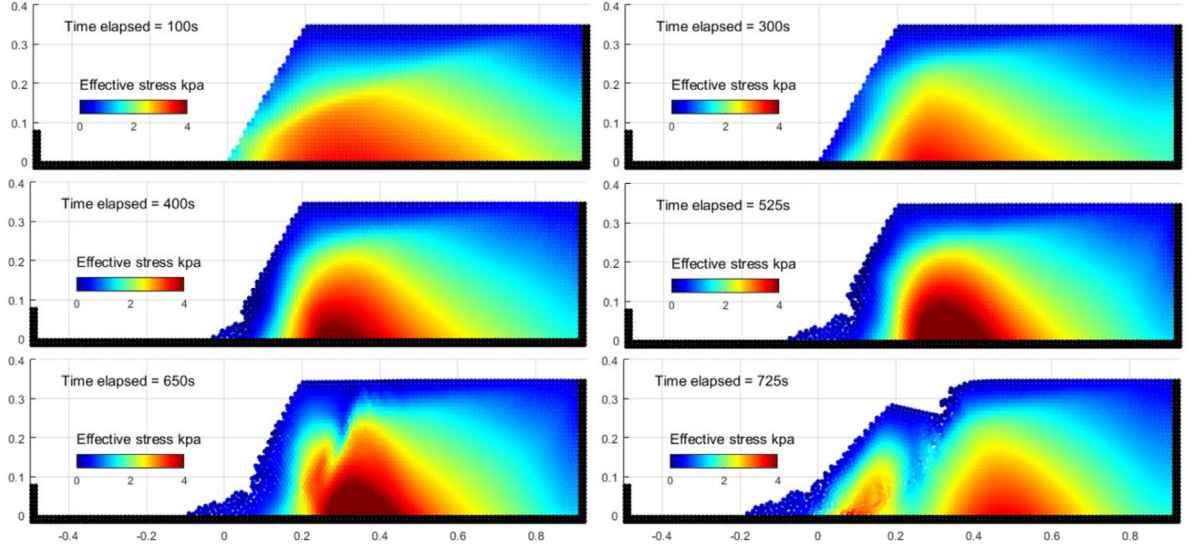


**Fig. 15.** Effective stress change during the erosion process.

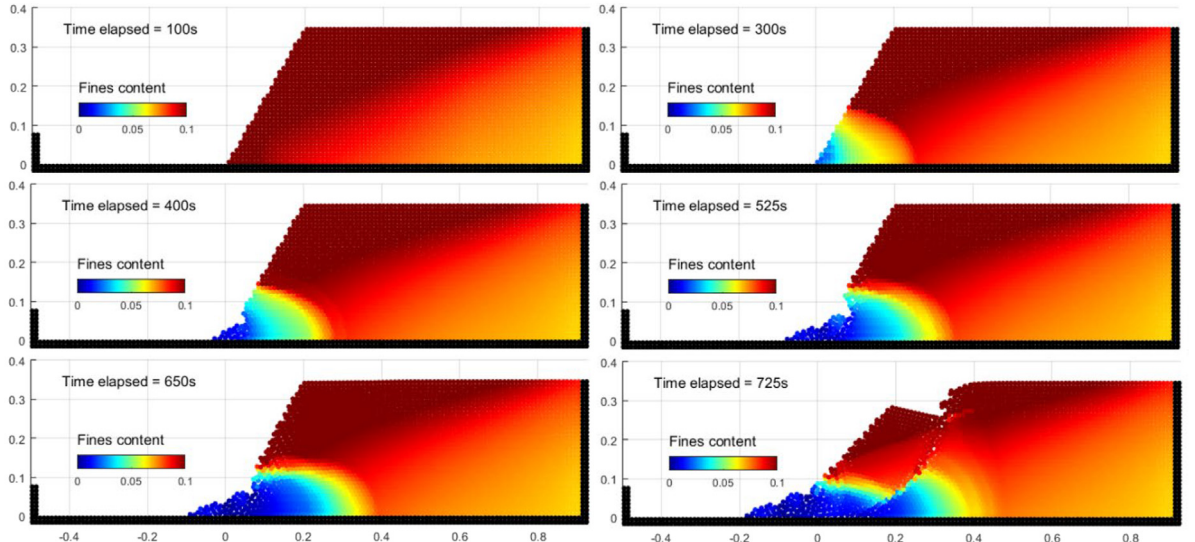


**Fig. 16.** Fines content change during the erosion process.

embankment toe, leading to a significant mass loss and fines content reduction around this zone. On the other hand, the concentration around the slope toe shows a reduction trend, indicating the clogging phenomenon within the embankment and preventing fluidised particles from being transported to this zone. It is worth noting that the presented stable distribution of concentration within the embankment could only be achieved after adopting the proposed concentration regularisation technique, which is again applied every 5000 computational steps. As the seepage erosion progresses, the eroded zone enlarges and retreats towards the embankment body, as shown in Fig. 16. The ultimate fines content in this zone can reach zero value, indicating that all the fines were eroded from the soil. This causes a significant reduction in the shear strength of the soil by altering the cohesion and friction angle, thanks to the proposed suction/erosion-dependent constitutive model. The loss of the soil strength at the embankment toe removes the embankment support, leading to the collapse of the embankment. Compared to the experiment, the evolution of fines content somewhat replicates the failure mechanisms observed in the experiment.

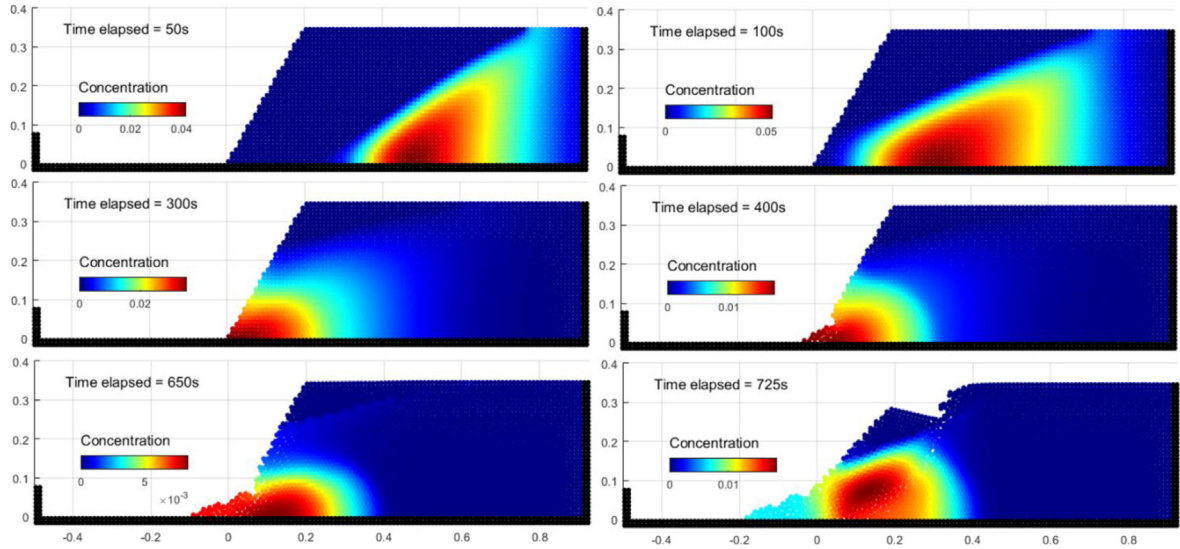


**Fig. 17.** Concentration change during the erosion process.

For example, the distribution of fines content at 400 s indicates the local failure at the embankment toe, whilst that at 400 s – 650 s shows an overhang zone on the upper part of the embankment surface. Unfortunately, the constitutive model proposed in this paper, although it can account for the shear strength reduction due to mass loss, is not enough to fully describe these complicated mechanisms of eroded soils, thus failing to capture the overhanging failure mechanism observed in the experiment. This observation suggests that more advanced constitutive models are still required to effectively account for the influence of mass loss on the shear strength of the eroded soils, and this will be further explored in future works. Nevertheless, the test presented in this section demonstrated that our proposed SPH framework has excellent capabilities to predict seepage-induced internal erosion and post-failure behaviour of soils compared to experimental results. Any advanced constitutive models proposed in the future can be straightforwardly incorporated into the current framework to improve its predictive capability.

The evolution of field quantities, including pore water pressure, fines content, concentration, cohesion and friction, at three specific locations inside the embankment, at the toe and close to its crest top (see Fig. 11), are recorded and presented in Fig. 18 to provide a better understand the mechanisms triggering embankment failure. The mass loss occurs as soon as the seepage flow reaches these locations and the critical hydraulic gradient is reached, as shown in Fig. 18(a). The fines content at the “inside” location experiences a rapid reduction during the transient seepage flow process and soon becomes stable, suggesting that the steady-state seepage flow condition at this location was soon established. On the other hand, the fines content at the “toe” location experiences a continuous mass loss until reaching a minimum erodible fines content (i.e., from  $k$  to  $l$  in the figure), suggesting that the slope toe was continuously subjected to a high hydraulic seepage gradient, which is always above the critical hydraulic gradient necessary for triggering internal erosion. In contrast, the “top” location resides within the unsaturated zone. Thus, the fines content remains unchanged until the embankment completely collapses, leading to a significant relocation of the “top” measuring point to a location where the seepage flow passes through, thus subsequently experiencing a negligible mass loss. The evolution of pore-water pressure at these locations is shown in Fig. 18(b). The pore water pressure increases across all measuring points during the transient seepage flow until the steady-state seepage flow condition is reached at around 250 s. Some minor variations in the pore-water at these locations after ~400 s can be attributed to the influence of embankment failure, causing changes to the excess pore-water pressure and the position of these measuring points. The suction (negative pore water pressure) reduces subsequently causes suction-dependent cohesion to reduce at all measuring points and dismiss at the toe and inside measuring points located inside the fully saturated zone, as shown in Fig. 18(c). Since the top measuring point is always located in the unsaturated zone, the pore water pressure remains negative, thus experiencing minimal suction strength loss. The loss of suction-dependent strength leads to the overall reduction of total cohesion, as shown in

**Fig. 18(d).** All suction-dependent strength at the slope toe and within the fully saturated zone inside the embankment was lost after  $\sim 100$  s. However, the embankment remains stable and has no signs of failure. It is noted that the friction angle is assumed to be independent of the suction in this simulation.

The influence of internal erosion on soil shear strength was visible at the inside location after  $\sim 50$  s, while that at the toe location can be observed after 100 s, as evidenced in **Fig. 18(d)** & (e). At the inside location, both apparent cohesion and apparent friction experience a short drop after  $\sim 50$  s until the fines content at this location reaches a stable value after  $\sim 100$  s. Since there is no change in the fines content afterwards, these shear strengths remain unchanged throughout the simulation. On the other hand, the apparent cohesion and friction angle at the toe location continuously reduces with the fines content loss to their residual values, as shown in **Fig. 18(d)**. The significant loss of soil strength at the slope toe subsequently causes local failure at this zone (at  $m$  around 400 s, see also **Fig. 13**) and eventually triggers the entire embankment to collapse. Note that the increase in the total suction after the embankment collapsed at  $\sim 650$  s, as shown in **Fig. 18(d)**, is due to the contribution from the suction, as evidenced in **Fig. 18(c)**. Finally, **Fig. 18(f)** shows the evolution of concentration at measuring points. Similar mechanisms observed in the 1D infiltration/erosion test, the transportation of fluidised particles from the upstream to the downstream of the embankment causes the concentration at the inside and toe locations to increase and reaches their peak values. After that, they gradually reduce due to the clogging issue caused by internal erosion upstream of the embankment. To this end, it is concluded from this test that internal erosion plays a dominant role in causing the deterioration of soil strength and could potentially lead to the instability of the earth structures such as the embankment in this study.

#### 4.7. Parametric investigations

This section investigates the influence of critical hydraulic gradient on seepage erosion-induced embankment collapse. In this investigation, we repeat the test performed in Section 4.6 by changing the critical hydraulic gradient to 0.25 and 0.5. **Fig. 19** shows the evolution of fines content under different critical hydraulic gradients. It can be seen that, compared to the results of  $i_c = 0.35$ , severe mass loss occurs during both transient and steady seepage flow when  $i_c = 0.25$ . This result suggests that a smaller critical hydraulic gradient accelerates the deterioration of soil strength, causing the embankment to collapse earlier. Under a large critical hydraulic gradient of  $i_c = 0.5$ , mass loss only occurs at the toe during steady seepage flow. However, it cannot trigger the backward erosion process and the entire collapse of the embankment. That is because the current hydraulic seepage gradients at the toe are consistently below the critical hydraulic gradient  $i_c = 0.5$ . Therefore, the critical hydraulic gradient plays a key role in triggering the erosion process and collapsing of the embankment.

Next, the influence of fluid bulk modulus is investigated. It is commonly known that it is not practical to adopt the actual fluid bulk modulus in modelling coupled problems using the explicit time integration method because it can result in a very small time step, leading to a substantial computational cost. As a result, a smaller fluid bulk modulus is commonly adopted [112]. In this investigation, we repeat the above embankment failure test using fluid bulk moduli of  $K_f = 1 \times 10^5$  Pa and  $K_f = 1 \times 10^6$  Pa. The corresponding time step was  $1 \times 10^{-4}$  s and  $4 \times 10^{-5}$  s, respectively. It is noted that the critical hydraulic gradient in these two tests was set to  $i_c = 0.25$  for the investigation purpose. **Fig. 20** compares two cases for the evolution of pore water pressure during the post-failure process of the embankment. The change in the fluid bulk modulus produces almost the same numerical results, except for some discrepancies in the development of the shear band near the top surface. Therefore, it is reasonable to assume that similar results can be achieved using larger or even the real water bulk modulus.

### 5. Conclusions

In this study, a general mathematical model was proposed to describe complex phase interactions and mass exchanges among five phases generated by the seepage erosion process in saturated/unsaturated porous media. The proposed mathematical model was essentially developed by further extending the mixture theory to account for the influence of mass loss due to erosion and mass gained due to deposition, which is described by empirical laws. By considering a five-phase system, the governing equations for fines content and concentration are automatically derived from mass conservation equations, providing a consistent mathematical model for describing the erosion process. A simple suction/erosion-dependent elastoplastic constitutive model was also proposed to account for the influences of suction and mass loss on the shear strength of soils. The newly proposed mathematical model was

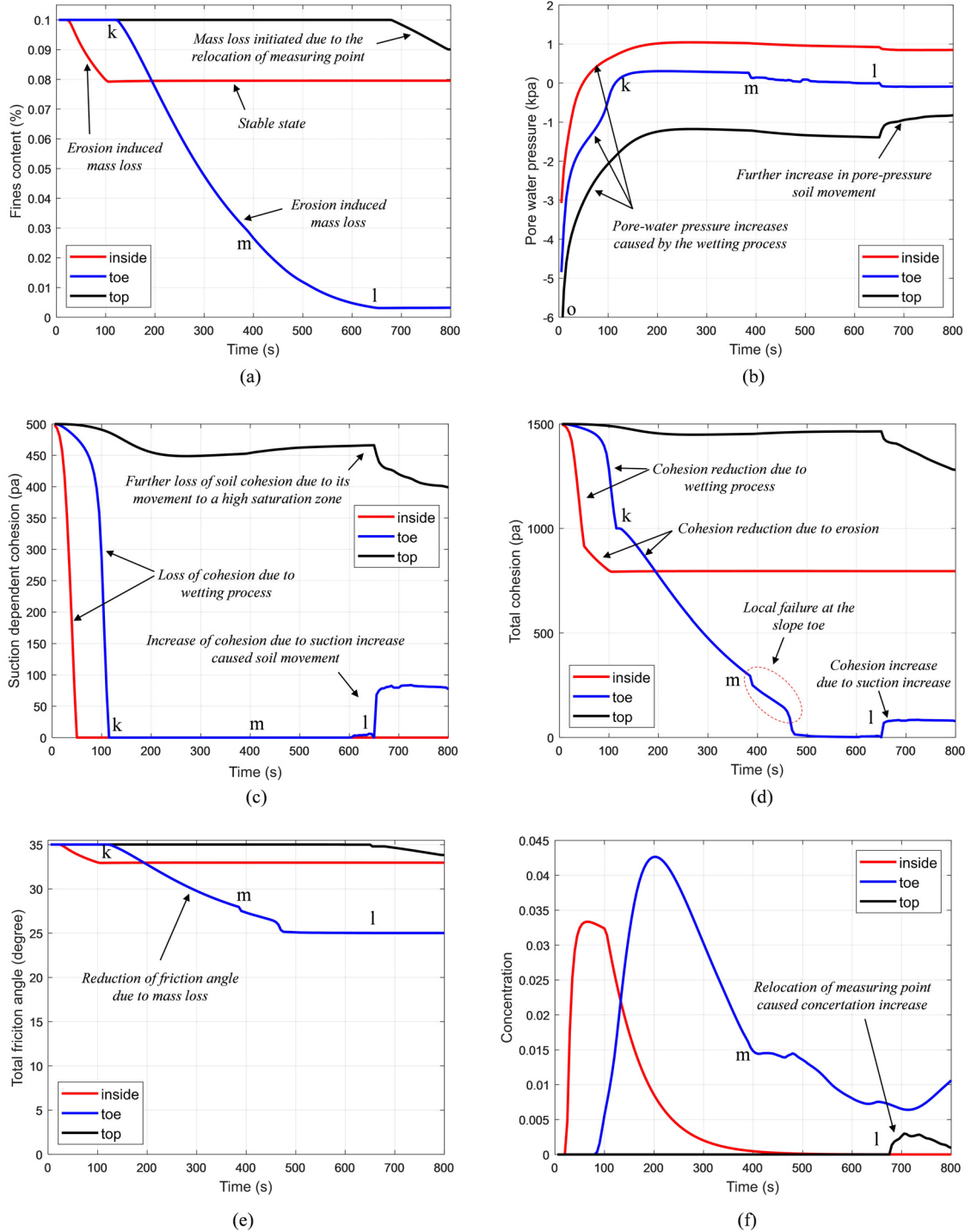
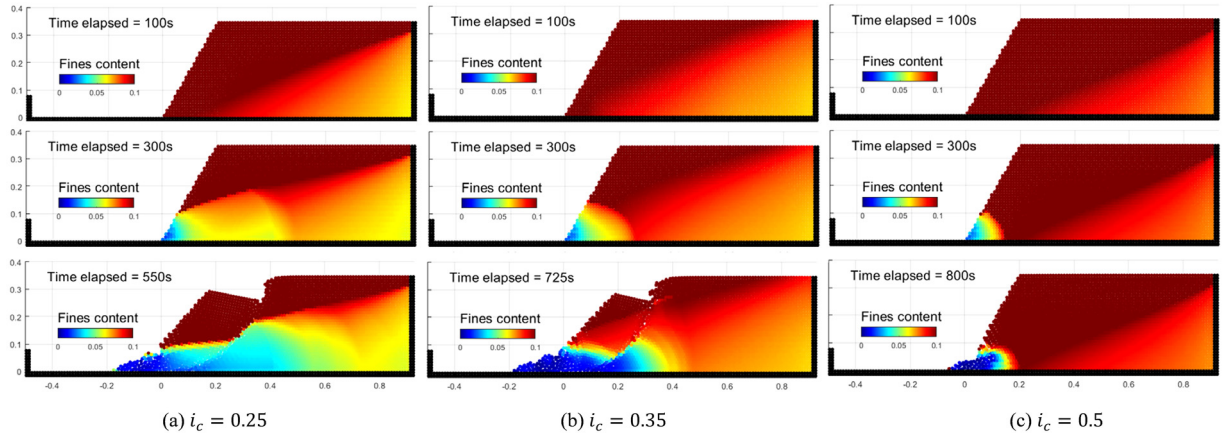
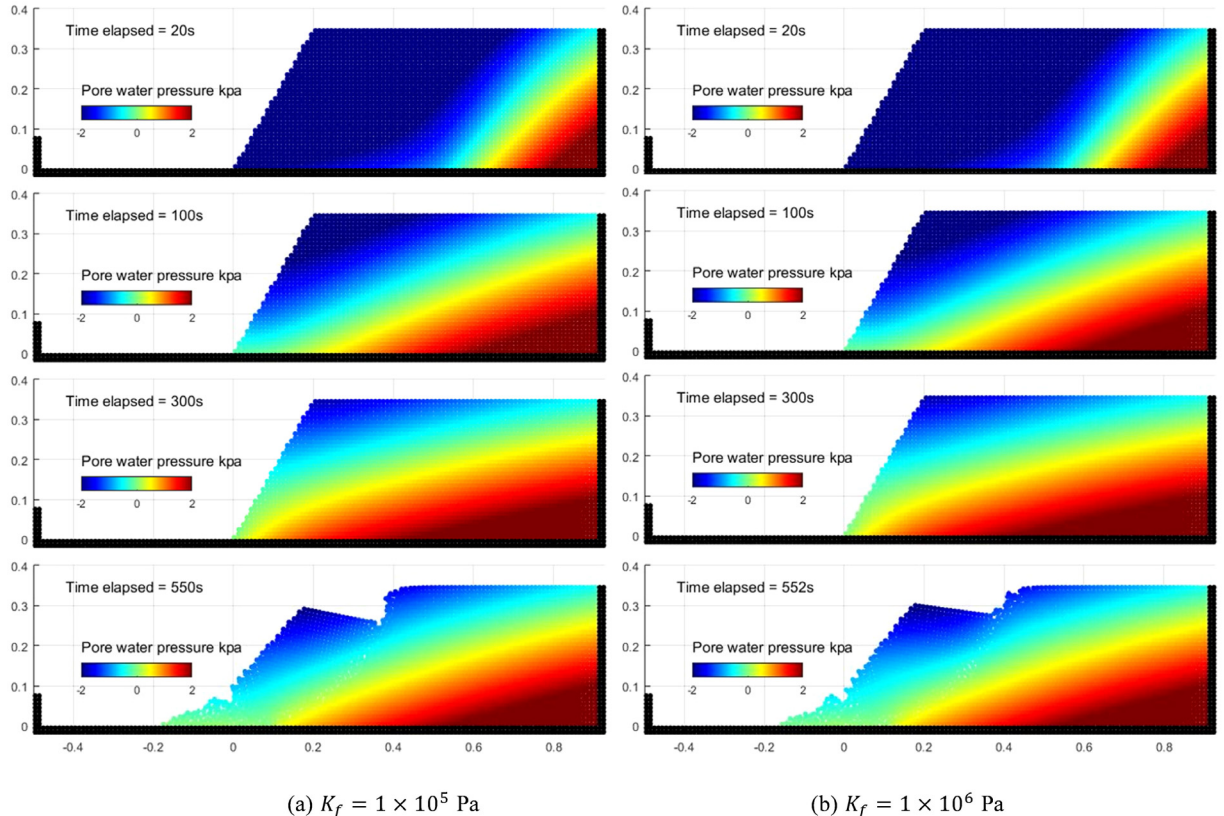


Fig. 18. Evolution of variables during seepage erosion at different locations.

subsequently solved by a robust and stabilised SPH computational framework and successfully used to simulate several challenging problems involving seepage erosion. Throughout this paper, it is shown that the proposed SPH-erosion framework can effectively capture the influence of erosion and deposition on the transient seepage



**Fig. 19.** Influence of critical hydraulic gradient on the seepage erosion-induced embankment failure.



**Fig. 20.** Influence of fluid bulk modulus tested on the pore-water pressure evolution during the post-failure process of the embankment.

flows and our numerical results are comparable to the experiment as well as other results reported in the literature. Furthermore, for the first time, the proposed SPH-erosion framework could capture the entire seepage-induced internal erosion and subsequent collapse process of an embankment observed in the experiment, and the numerical results showed qualitative agreement with the experiment. To further improve the predictive capability of the proposed computational framework, research efforts are required to properly describe the mass exchange laws, which are mostly based on empirical laws at the moment. More advanced constitutive models are also required for

better descriptions of the influence of mass loss on the shear strength reduction of soils. These are beyond the scope of this paper and will be investigated in future works.

## Declaration of competing interest

The authors declare that they have no known competing financial interests or personal relationships that could have appeared to influence the work reported in this paper.

## Data availability

No data was used for the research described in the article.

## Acknowledgements

The authors gratefully acknowledge the financial support from the Australian Research Council via Discovery Projects DP190102779 (Bui & Nguyen) and FT200100884 (Bui). Part of this research was undertaken with the assistance of resources and services from the National Computational Infrastructure (NCI), supported by the Australian Government. The author also gratefully thanks the support of the China Scholarship Council (CSC).

## References

- [1] L.M. Zhang, Q. Chen, Seepage failure mechanism of the gouhou rockfill dam during reservoir water infiltration, *Soils Found.* 46 (2006) 557–568.
- [2] R. Fell, J.-J. Fry, The state of the art of assessing the likelihood of internal erosion of embankment dams, water retaining structures and their foundations, *Internal erosion of dams and their foundations*, 2007, pp. 9–32.
- [3] M. Foster, R. Fell, M. Spannagle, The statistics of embankment dam failures and accidents, *Can. Geotech. J.* 37 (2000) 1000–1024.
- [4] A.W. Skempton, J.M. Brogan, Experiments on piping in sandy gravels, *Géotechnique* 44 (1994) 449–460.
- [5] K. Terzaghi, R.B. Peck, G. Mesri, *Soil Mechanics in Engineering Practice*, John Wiley & Sons, 1996.
- [6] D.S. Chang, L.M. Zhang, Critical hydraulic gradients of internal erosion under complex stress states, *J. Geotech. Geoenviron.* 139 (2013) 1454–1467.
- [7] C. Nguyen, N. Benahmed, E. Andò, L. Sibille, P. Philippe, Experimental investigation of microstructural changes in soils eroded by suffusion using X-ray tomography, *Acta Geotech.* 14 (2019) 749–765.
- [8] F. Bianchi, F.K. Wittel, M. Thielmann, P. Trtik, H.J. Herrmann, Tomographic study of internal erosion of particle flows in porous media, *Transp. Porous Media* 122 (2018) 169–184.
- [9] H. Mori, *SPH Method To Simulate River Levee Failures*, University of Cambridge, 2008.
- [10] G.A. Fox, M.L. Chu-Agor, G.V. Wilson, Erosion of noncohesive sediment by ground water seepage: Lysimeter experiments and stability modeling, *Soil Sci. Soc. Am. J.* 71 (2007) 1822–1830.
- [11] H.H. Bui, G.D. Nguyen, A coupled fluid-solid SPH approach to modelling flow through deformable porous media, *Int. J. Solids Struct.* 125 (2017) 244–264.
- [12] K. Horikoshi, A. Takahashi, Suffusion-induced change in spatial distribution of fine fractions in embankment subjected to seepage flow, *Soils Found.* 55 (2015) 1293–1304.
- [13] I. Vardoulakis, M. Stavropoulou, P. Papanastasiou, Hydro-mechanical aspects of the sand production problem, *Transp. Porous Media* 22 (1996) 225–244.
- [14] H. Steeb, S. Diebels, A thermodynamic-consistent model describing growth and remodeling phenomena, *Comput. Mater. Sci.* 28 (2003) 597–607.
- [15] H. Steeb, S. Diebels, I. Vardoulakis, Modeling internal erosion in porous media, *Comput. Appl. Geotech. Eng.* (2007) 1–10.
- [16] J. Yang, Z.-Y. Yin, F. Laouafa, P.-Y. Hicher, Internal erosion in dike-on-foundation modeled by a coupled hydromechanical approach, *Int. J. Numer. Anal. Methods Geomech.* 43 (2019) 663–683.
- [17] J. Yang, Z.-Y. Yin, F. Laouafa, P.-Y. Hicher, Three-dimensional hydromechanical modeling of internal erosion in dike-on-foundation, *Internat. J. Numerical Analytical Methods Geomech.* 44 (2020) 1200–1218.
- [18] X. Lei, Z. Yang, S. He, E. Liu, H. Wong, X. Li, Numerical investigation of rainfall-induced fines migration and its influences on slope stability, *Acta Geotech.* 12 (2017) 1431–1446.
- [19] L. Zhang, F. Wu, H. Zhang, L. Zhang, J. Zhang, Influences of internal erosion on infiltration and slope stability, *Bull. Eng. Geol. Environ.* 78 (2019) 1815–1827.
- [20] J. Yang, Z.-Y. Yin, F. Laouafa, P.-Y. Hicher, Modeling coupled erosion and filtration of fine particles in granular media, *Acta Geotech.* 14 (2019) 1615–1627.
- [21] J. Yang, Z.-Y. Yin, F. Laouafa, P.-Y. Hicher, Analysis of suffusion in cohesionless soils with randomly distributed porosity and fines content, *Comput. Geotech.* 111 (2019) 157–171.
- [22] X. Lei, S. He, X. Chen, H. Wong, L. Wu, E. Liu, A generalized interpolation material point method for modelling coupled seepage-erosion-deformation process within unsaturated soils, *Adv. Water Resour.* (2020) 103578.

- [23] H.H. Bui, R. Fukagawa, K. Sako, S. Ohno, Lagrangian meshfree particles method (SPH) for large deformation and failure flows of geomaterial using elastic–plastic soil constitutive model, *Int. J. Numer. Anal. Methods Geomech.* 32 (2008) 1537–1570.
- [24] A.H. Fávero Neto, R.I. Borja, Continuum hydrodynamics of dry granular flows employing multiplicative elastoplasticity, *Acta Geotech.* 13 (2018) 1027–1040.
- [25] H.H. Bui, R. Fukagawa, K. Sako, J.C. Wells, Slope stability analysis and discontinuous slope failure simulation by elasto-plastic smoothed particle hydrodynamics (SPH), *Géotechnique* 61 (2011) 565–574.
- [26] H.H. Bui, G.D. Nguyen, Smoothed particle hydrodynamics (SPH) and its applications in geomechanics: From solid fracture to granular behaviour and multiphase flows in porous media, *Comput. Geotech.* 138 (2021) 104315.
- [27] Y. Lian, H.H. Bui, G.D. Nguyen, S. Zhao, A. Haque, A computationally efficient SPH framework for unsaturated soils and its application to predicting the entire rainfall-induced slope failure process, *Géotechnique* 1–19, <http://dx.doi.org/10.1680/jgeot.21.00349>.
- [28] D.S. Morikawa, M. Asai, Soil-water strong coupled ISPH based on u- w- p formulation for large deformation problems, *Comput. Geotech.* 142 (2022) 104570.
- [29] C. Chalk, M. Pastor, J. Peakall, D. Borman, P. Sleigh, W. Murphy, R. Fuentes, Stress-particle smoothed particle hydrodynamics: An application to the failure and post-failure behaviour of slopes, *Comput. Method Appl. M* 366 (2020) 113034.
- [30] W. Chen, T. Qiu, Simulation of earthquake-induced slope deformation using SPH method, *Int. J. Numer. Anal. Methods Geomech.* 38 (2014) 297–330.
- [31] M. Pastor, B. Haddad, G. Sorbino, S. Cuomo, V. Dremptic, A depth-integrated, coupled SPH model for flow-like landslides and related phenomena, *Int. J. Numer. Anal. Methods Geomech.* 33 (2009) 143–172.
- [32] M. Pastor, T. Blanc, B. Haddad, S. Petrone, M.S. Morles, V. Dremptic, D. Issler, G. Crosta, L. Cascini, G. Sorbino, Application of a SPH depth-integrated model to landslide run-out analysis, *Landslides* 11 (2014) 793–812.
- [33] S.M. Tayyebi, M. Pastor, A.L. Yifru, V.K. Thakur, M.M. Stickle, Two-phase SPH–FD depth-integrated model for debris flows: application to basal grid brakes, *Géotechnique* (2021) 1–16.
- [34] A.H. Fávero Neto, A. Askarinejad, S.M. Springman, R.I. Borja, Simulation of debris flow on an instrumented test slope using an updated Lagrangian continuum particle method, *Acta Geotech.* 15 (2020) 2757–2777.
- [35] B. Sheikh, T. Qiu, A. Ahmadipur, Comparison of SPH boundary approaches in simulating frictional soil–structure interaction, *Acta Geotech.* 16 (2021) 2389–2408.
- [36] E. Yang, H.H. Bui, G.D. Nguyen, C.E. Choi, C.W.W. Ng, H. De Sterck, A. Bouazza, Numerical investigation of the mechanism of granular flow impact on rigid control structures, *Acta Geotech.* 16 (2021) 2505–2527.
- [37] D.S. Morikawa, M. Asai, Coupling total Lagrangian SPH–EISPH for fluid–structure interaction with large deformed hyperelastic solid bodies, *Comput. Method Appl. M* 381 (2021) 113832.
- [38] M. Asai, Y. Li, B. Chandra, S. Takase, Fluid–rigid-body interaction simulations and validations using a coupled stabilized ISPH–DEM incorporated with the energy-tracking impulse method for multiple-body contacts, *Comput. Method Appl. M* 377 (2021) 113681.
- [39] W. Hu, M. Rakhsa, L. Yang, K. Kamrin, D. Negrut, Modeling granular material dynamics and its two-way coupling with moving solid bodies using a continuum representation and the SPH method, *Comput. Method Appl. M* 385 (2021) 114022.
- [40] Z.-F. Meng, A.M. Zhang, J.-L. Yan, P.-P. Wang, A. Khayyer, A hydroelastic fluid–structure interaction solver based on the Riemann-SPH method, *Comput. Method Appl. M* 390 (2022) 114522.
- [41] Y. Wang, H.H. Bui, G.D. Nguyen, P. Ranjith, A new SPH-based continuum framework with an embedded fracture process zone for modelling rock fracture, *Int. J. Solids Struct.* 159 (2019) 40–57.
- [42] Y. Wang, H.T. Tran, G.D. Nguyen, P.G. Ranjith, H.H. Bui, Simulation of mixed-mode fracture using SPH particles with an embedded fracture process zone, *Int. J. Numer. Anal. Methods Geomech.* 44 (2020) 1417–1445.
- [43] Y. Lian, H.H. Bui, G.D. Nguyen, H.T. Tran, A. Haque, A general SPH framework for transient seepage flows through unsaturated porous media considering anisotropic diffusion, *Comput. Method Appl. M* 387 (2021) 114169.
- [44] A. Khayyer, H. Gotoh, Y. Shimizu, K. Gotoh, H. Falahaty, S. Shao, Development of a projection-based SPH method for numerical wave flume with porous media of variable porosity, *Coast. Eng.* 140 (2018) 1–22.
- [45] C. Peng, G. Xu, W. Wu, H. s. Yu, C. Wang, Multiphase SPH modeling of free surface flow in porous media with variable porosity, *Comput. Geotech.* 81 (2017) 239–248.
- [46] Y. Zhao, R.I. Borja, A continuum framework for coupled solid deformation–fluid flow through anisotropic elastoplastic porous media, *Comput. Method Appl. M* 369 (2020) 113225.
- [47] Y.-F. Jin, Z.-Y. Yin, Two-phase PFEM with stable nodal integration for large deformation hydromechanical coupled geotechnical problems, *Comput. Method Appl. M* 392 (2022) 114660.
- [48] H. Xiong, Z.-Y. Yin, J. Zhao, Y. Yang, Investigating the effect of flow direction on suffusion and its impacts on gap-graded granular soils, *Acta Geotech.* 16 (2021) 399–419.
- [49] H. Tao, J. Tao, Quantitative analysis of piping erosion micro-mechanisms with coupled CFD and DEM method, *Acta Geotech.* 12 (2017) 573–592.
- [50] O.C. Zienkiewicz, A. Chan, M. Pastor, B. Schrefler, T. Shiomi, Computational Geomechanics, Citeseer, 1999.
- [51] A. Yerro Colom, MPM modelling of landslides in brittle and unsaturated soils, 2015.
- [52] H.H. Bui, R. Fukagawa, An improved SPH method for saturated soils and its application to investigate the mechanisms of embankment failure: Case of hydrostatic pore-water pressure, *Int. J. Numer. Anal. Methods Geomech.* 37 (2013) 31–50.
- [53] S. Kularathna, W. Liang, T. Zhao, B. Chandra, J. Zhao, K. Soga, A semi-implicit material point method based on fractional-step method for saturated soil, *Int. J. Numer. Anal. Methods Geomech.* 45 (2021) 1405–1436.
- [54] P. Lade, R. De Boer, The concept of effective stress for soil concrete and rock, *Géotechnique* 47 (1997) 61–78.
- [55] R.I. Borja, On the mechanical energy and effective stress in saturated and unsaturated porous continua, *Int. J. Solids Struct.* 43 (2006) 1764–1786.

- [56] R. Uzuoka, R.I. Borja, Dynamics of unsaturated poroelastic solids at finite strain, *Int. J. Numer. Anal. Methods Geomech.* 36 (2012) 1535–1573.
- [57] B. Schrefler, L. Simoni, L. Xikui, O. Zienkiewicz, *Mechanics of Partially Saturated Porous Media, Numerical Methods and Constitutive Modelling in Geomechanics*, Springer, 1990, pp. 169–209.
- [58] A.W. Bishop, G. Blight, Some aspects of effective stress in saturated and partly saturated soils, *Geotechnique* 13 (1963) 177–197.
- [59] N. Khalili, F. Geiser, G. Blight, Effective stress in unsaturated soils: Review with new evidence, *Int. J. Geomech.* 4 (2004) 115–126.
- [60] R. Lewis, B. Schrefler, Finite element simulation of the subsidence of a gas reservoir undergoing a waterdrive, *Finite Elem. Fluids Wiley* (1982) 179–199.
- [61] G. Housby, The work input to an unsaturated granular material, *Géotechnique* 47 (1997) 193–196.
- [62] M. Nuth, L. Laloui, Effective stress concept in unsaturated soils: Clarification and validation of a unified framework, *Int. J. Numer. Anal. Methods Geomech.* 32 (2008) 771–801.
- [63] A. Gens, M. Sánchez, D. Sheng, On constitutive modelling of unsaturated soils, *Acta Geotech.* 1 (2006) 137–147.
- [64] B. Loret, N. Khalili, A three-phase model for unsaturated soils, *Int. J. Numer. Anal. Methods Geomech.* 24 (2000) 893–927.
- [65] R.I. Borja, A. Koliji, On the effective stress in unsaturated porous continua with double porosity, *J. Mech. Phys. Solids* 57 (2009) 1182–1193.
- [66] F. Oka, B. Shahbodagh, S. Kimoto, A computational model for dynamic strain localization in unsaturated elasto-viscoplastic soils, *Int. J. Numer. Anal. Methods Geomech.* 43 (2019) 138–165.
- [67] R. Lewis, B. Schrefler, The finite element method in the static and dynamic deformation and consolidation in porous media, 1998.
- [68] R. Bowen, *Theory of Mixtures, AC Eringen, Continuum Physics*, Academic Press, New York, 1976.
- [69] F. Oka, S. Kimoto, *Computational Modeling of Multiphase Geomaterials*, CRC Press, 2012.
- [70] M.T. van Genuchten, A closed-form equation for predicting the hydraulic conductivity of unsaturated soils, *Soil Sci. Am. J.* 44 (1980) 892–898.
- [71] J. Kozeny, Über kapillareleitung der wasser in boden, *R. Acad. Sci. Vienna, Proc. Class I* 136 (1927) 271–306.
- [72] P.C. Carman, *Flow of Gases Through Porous Media*, Butterworths Scientific Publications, London, 1956.
- [73] Z.-Y. Yin, J. Yang, F. Laouafa, P.-Y. Hicher, A framework for coupled hydro-mechanical continuous modelling of gap-graded granular soils subjected to suffusion, *Euro. J. Environ. Civ. Eng.* (2020) 1–22.
- [74] D. Sterpi, Effects of the erosion and transport of fine particles due to seepage flow, *Int. J. Geomech.* 3 (2003) 111–122.
- [75] A. Cividini, S. Bonomi, G.C. Vignati, G. Gioda, Seepage-induced erosion in granular soil and consequent settlements, *Int. J. Geomech.* 9 (2009) 187–194.
- [76] A. Cividini, G. Gioda, Finite-element approach to the erosion and transport of fine particles in granular soils, *Int. J. Geomech.* 4 (2004) 191–198.
- [77] A. Schaufler, C. Becker, H. Steeb, Infiltration processes in cohesionless soils, *ZAMM-J. Appl. Math. Mech. Z. Angew. Math. Mech.* 93 (2013) 138–146.
- [78] T. Khalil, N. Saiouri, B. Muresan, P.Y. Hicher, Internal erosion of chemically reinforced granular materials: a mathematical modeling approach, *Int. J. Numer. Anal. Methods Geomech.* 37 (2013) 491–502.
- [79] A. Yerro, E. Alonso, N. Pinyol, The material point method for unsaturated soils, *Géotechnique* 65 (2015) 201–217.
- [80] A. Yerro, E. Alonso, N. Pinyol, Run-out of landslides in brittle soils, *Comput. Geotech.* 80 (2016) 427–439.
- [81] F. Zabala, E. Alonso, Progressive failure of Aznalcóllar dam using the material point method, *Géotechnique* 61 (2011) 795–808.
- [82] C. Chen, L.M. Zhang, D.S. Chang, Stress-strain behavior of granular soils subjected to internal erosion, *J. Geotech. Geoenvir.* 142 (2016) 06016014.
- [83] L. Scholtès, P.-Y. Hicher, L. Sibille, Multiscale approaches to describe mechanical responses induced by particle removal in granular materials, *C. R. Méc.* 338 (2010) 627–638.
- [84] N.H. Nguyen, H.H. Bui, G.D. Nguyen, Effects of material properties on the mobility of granular flow, *Granul. Matter* 22 (2020) 1–17.
- [85] Y.-F. Jin, Z.-Y. Yin, Enhancement of backtracking search algorithm for identifying soil parameters, *Internat. J. Numerical Anal. Methods Geomech.* 44 (2020) 1239–1261.
- [86] Z.-Y. Yin, Y.-F. Jin, J.-S. Shen, P.-Y. Hicher, Optimization techniques for identifying soil parameters in geotechnical engineering: comparative study and enhancement, *Internat. J. Numerical Anal. Methods Geomech.* 42 (2018) 70–94.
- [87] Z.-Y. Yin, J. Zhao, P.-Y. Hicher, A micromechanics-based model for sand-silt mixtures, *Int. J. Solids Struct.* 51 (2014) 1350–1363.
- [88] Z.-Y. Yin, H.-W. Huang, P.-Y. Hicher, Elastoplastic modeling of sand-silt mixtures, *Soils Found.* 56 (2016) 520–532.
- [89] E.A. de Souza Neto, D. Peric, D.R. Owen, *Computational Methods for Plasticity: Theory and Applications*, John Wiley & Sons, 2011.
- [90] G.D. Nguyen, H.H. Bui, A thermodynamics- and mechanism-based framework for constitutive models with evolving thickness of localisation band, *Int. J. Solids Struct.* 187 (2020) 100–120.
- [91] G.D. Nguyen, G.T. Housby, A coupled damage-plasticity model for concrete based on thermodynamic principles: Part I: model formulation and parameter identification, *Int. J. Numer. Anal. Methods Geomech.* 32 (2008) 353–389.
- [92] R. De Borst, M.A. Crisfield, J.J. Remmers, C.V. Verhoosel, *Nonlinear Finite Element Analysis of Solids and Structures*, John Wiley & Sons, 2012.
- [93] H.T. Tran, Y. Wang, G.D. Nguyen, J. Kodikara, M. Sanchez, H.H. Bui, Modelling 3D desiccation cracking in clayey soils using a size-dependent SPH computational approach, *Comput. Geotech.* 116 (2019) 103209.
- [94] L.A. Le, G.D. Nguyen, H.H. Bui, A.H. Sheikh, A. Kotousov, Localised failure mechanism as the basis for constitutive modelling of geomaterials, *Internat. J. Engrg. Sci.* 133 (2018) 284–310.

- [95] L.A. Le, G.D. Nguyen, H.H. Bui, A.H. Sheikh, A. Kotousov, Incorporation of micro-cracking and fibre bridging mechanisms in constitutive modelling of fibre reinforced concrete, *J. Mech. Phys. Solids* 133 (2019) 103732.
- [96] Y.-F. Jin, Z.-X. Wu, Z.-Y. Yin, J. Shen, Estimation of critical state-related formula in advanced constitutive modeling of granular material, *Acta Geotech.* 12 (2017) 1329–1351.
- [97] D. Muir Wood, K. Maeda, E. Nukudani, Modelling mechanical consequences of erosion, *Géotechnique* 60 (2010) 447–457.
- [98] E. Papamichos, Erosion and multiphase flow in porous media: Application to sand production, *Euro. J. Environ. Civ. Eng.* 14 (2010) 1129–1154.
- [99] G.-R. Liu, M.B. Liu, Smoothed particle hydrodynamics: a meshfree particle method, *World Sci.* (2003).
- [100] J.J. Monaghan, Smoothed particle hydrodynamics and its diverse applications, *Annu. Rev. Fluid Mech.* 44 (2012) 323–346.
- [101] L. Brookshaw, A method of calculating radiative heat diffusion in particle simulations, *Publ. Astron. Soc. Aust.* 6 (1985) 207–210.
- [102] P.W. Cleary, J.J. Monaghan, Conduction modelling using smoothed particle hydrodynamics, *J. Comput. Phys.* 148 (1999) 227–264.
- [103] P. Randles, L.D. Libersky, Smoothed particle hydrodynamics: some recent improvements and applications, *Comput. Method Appl. M* 139 (1996) 375–408.
- [104] J. Chen, J. Beraun, T. Carney, A corrective smoothed particle method for boundary value problems in heat conduction, *Internat. J. Numer. Methods Engrg.* 46 (1999) 231–252.
- [105] C.T. Nguyen, C.T. Nguyen, H.H. Bui, G.D. Nguyen, R. Fukagawa, A new SPH-based approach to simulation of granular flows using viscous damping and stress regularisation, *Landslides* 14 (2017) 69–81.
- [106] P. De Sampaio, A Petrov–Galerkin/modified operator formulation for convection–diffusion problems, *Internat. J. Numer. Methods Engrg.* 30 (1990) 331–347.
- [107] W. Shyy, A study of finite difference approximations to steady-state convection-dominated flow problems, *J. Comput. Phys.* 57 (1985) 415–438.
- [108] C.C. Yu, J.C. Heinrich, Petrov–Galerkin methods for the time-dependent convective transport equation, *Internat. J. Numer. Methods Engrg.* 23 (1986) 883–901.
- [109] W. Gardner, Some steady-state solutions of the unsaturated moisture flow equation with application to evaporation from a water table, *Soil Sci.* 85 (1958) 228–232.
- [110] X. Liu, F. Civan, Characterization and prediction of formation damage in two-phase flow systems, in: SPE Production Operations Symposium, OnePetro, 1993.
- [111] P. Cui, C. x. Guo, J. w. Zhou, M. h. Hao, F. g. Xu, The mechanisms behind shallow failures in slopes comprised of landslide deposits, *Eng. Geol.* 180 (2014) 34–44.
- [112] V. Galavi, Groundwater flow, fully coupled flow deformation and undrained analyses in PLAXIS 2D and 3D, *Plaxis Rep.* (2010).